Titre: Title:	Simulation of borehole thermal energy storage (BTES) systems using simplified methods
Auteurs: Authors:	Mohammadamin Ahmadfard, & Michel Bernier
Date:	2023
Type:	Article de revue / Article
Référence: Citation:	Ahmadfard, M., & Bernier, M. (2023). Simulation of borehole thermal energy storage (BTES) systems using simplified methods. Journal of Energy Storage, 73(D), 109240 (18 pages). https://doi.org/10.1016/j.est.2023.109240

Document publié chez l'éditeur officiel
Document issued by the official publisher

Titre de la revue: Journal Title:	Journal of Energy Storage (vol. 73, no. D)
Maison d'édition: Publisher:	Elsevier
URL officiel: Official URL:	https://doi.org/10.1016/j.est.2023.109240
Mention légale: Legal notice:	

Simulation of borehole thermal energy storage (BTES) systems using simplified methods

by

Mohammadamin Ahmadfard and Michel Bernier

Polytechnique Montréal

Department of Mechanical Engineering

Montréal, Canada

Accepted for publication in October 2023

Simulation of borehole thermal energy storage (BTES) systems using simplified methods

Mohammadamin Ahmadfard, Michel Bernier*
Polytechnique Montréal, Department of Mechanical Engineering
Montréal, Canada

Abstract

This paper presents two complementary approaches for simulating the thermal performance of borehole thermal energy storage (BTES) systems. The first approach uses the concepts of heat exchange and storage efficiencies as a function of the state-of-charge of the BTES. The second method employs a technique similar to thermal response factors used to model bore fields in ground-source heat pump systems. It utilizes non-dimensional average storage temperatures and bore field thermal resistances of the BTES over time. The two methods rely on numerical experiments to obtain the required performance curves. As shown through examples, the two approaches are relatively simple to use, and it is shown that they are in good agreement with the well-known duct ground storage model. In one of the examples, it is suggested that the design of a BTES could be performed using three successive thermal pulses, similar to the approach used to determine the length of vertical ground heat exchangers in a ground-source heat pump systems.

*Corresponding author

Keywords: Borehole Thermal Energy Storage, geothermal, efficiency, simulation, models

Introduction

Borehole thermal energy storage (BTES) systems use boreholes as heat exchangers to store and retrieve thermal energy in the ground for seasonal storage. The design of BTES systems is fundamentally different from regular borehole fields used with ground-source heat pump (GSHP) systems. First, boreholes are tightly packed, and borehole-to-borehole thermal interaction is much greater and most often beneficial. This implies that higher temperatures can be achieved. Secondly, the boreholes are generally positioned in a parallel-series arrangement to promote radial stratification, while they are typically piped in parallel in GSHP systems. Designing BTES systems is still a difficult task for design engineers, as it requires access to specific simulation tools that are relatively difficult to master. The objective of this paper is to propose simpler methods that could be routinely used.

One of the most successful BTES systems has been operating since 2007 at the Drake Landing Solar Community (DLSC) in Okotoks, Canada (Mesquita et al., 2017; Sibbitt et al., 2007, 2012a). This system, shown schematically in Figure 1, has been able to supply more than 90% of the space heating needs of 52 houses. In charging mode, heat from a solar collector array is injected into the center of the BTES at T_{in} and exists at the periphery at T_{out}, as shown in Figure 1. This creates a radial thermal stratification with a hot core and a warm periphery. In discharging mode, the flow is reversed and cold fluid enters at the periphery and gets progressively heated when flowing in six boreholes positioned in series before exiting from the BTES center. The BTES temperature, characterized here by its average temperature, T_s, is much greater than the undisturbed ground temperature, T_g, and the ambient temperature, T_{amb}. The total heat exchanged between the fluid and the BTES can either increase (or decrease in discharging mode) the ground's internal energy or be lost in the form of heat losses from the top, bottom, and side surfaces. Low system efficiency and high initial installation costs are the primary barriers to BTES system development (Hughes, 2008), whereas low operational cost is the primary advantage.

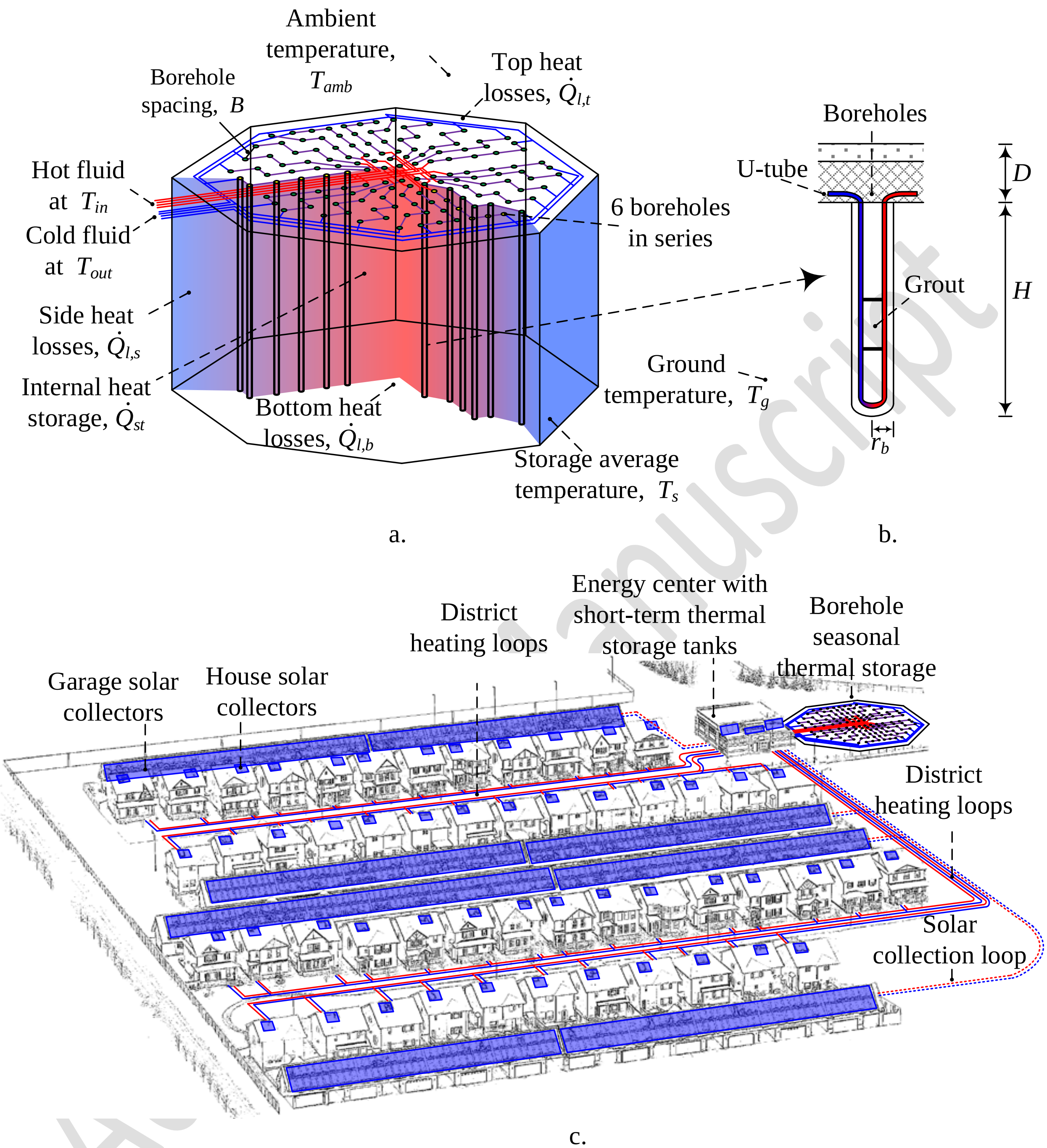

Figure 1: Schematic representation of the BTES system at the Drake Landing Solar Community

Literature review

As noted by Gehlin (2016), who studied BTES installations around the world, there is no standard definition for BTES systems. However, it is generally agreed that some form of intentional thermal storage in the ground for long periods is required to qualify as a BTES system. Lanahan and Tabares-Velasco (2017) reviewed the literature on BTES systems and provided guidance on component and system modeling tools. Other studies have recently focused on BTES modeling, and the reader is referred to the following investigations for more details: Schmidt and Hellström (2005), Cho and Mirianhosseinabadi (2013), Andresen (2014), Gao et al. (2015), Schulte et al. (2016), Nilsson (2020), and Xu (2020). As an example, the paper by Welsch et al. (2016) investigates the impact of design parameters like fluid inlet temperature, bore field layout, and reservoir rock properties on the functional performance of medium-deep boreholes for seasonal heat storage. Through numerical simulations, they find that properly dimensioned systems in suitable geological conditions are well-suited for seasonal heat storage, especially larger systems with a potential recovery rate of up to 83%. Adjusting supply temperatures and increasing the storage charging temperature can further enhance borehole thermal energy storage (BTES) efficiencies. Optimizing borehole spacing and number, along with borehole length, improves storage capacity and efficiency.

Hadorn et al. (1988) provided a historical perspective on seasonal heat storage, including BTES systems. In his work, several key concepts such as heat transfer capacity, heat storage capacity, equivalent cycle index, and storage energy efficiency are defined. One of the most important metrics is seasonal energy efficiency. Applied to a BTES operating on an annual cycle, the BTES efficiency, η_{BTES}, is defined as follows:

$$\eta_{BTES} = \frac{E_{ext}}{E_{inj}} = \frac{E_{ext}}{E_{ext} + E_l} = \frac{\int_0^t \dot{m}' C_p{}' (T'_{out} - T'_{in})\, dt}{\int_0^t \dot{m} C_p (T_{out} - T_{in}) dt} = 1 - \frac{E_l}{E_{inj}} \tag{1}$$

where E_{inj} is the injected energy, E_{ext} is the extracted energy, and E_l is the energy lost in an annual cycle. In this equation, $\dot{m}$ and $\dot{m}'$ are the flow rates, C_p and $C_p{}'$ are the fluid thermal capacities, T_{in} and T'_{in} and T_{out} and T'_{out} are inlet and outlet fluid temperatures in charging and discharging modes, respectively, and t is the time period, which is typically one year. E_l is equal to $UA\left(T_{avg} - T_e\right)t$, where $\left(T_{avg} - T_e\right)$ is the annual average temperature difference between the storage and the environment, U is the equivalent heat loss factor, and A is the storage envelope surface area.

Pahud (2002) used Equation 1 to evaluate BTES efficiencies. He noted that for low-temperature BTES systems, the efficiency can reach 60 to 90% because of reduced heat losses. In fact, E_l depends on the storage envelope surface area, and E_{inj} depends on volume. Thus, by increasing the storage surface, the E_l/E_{inj} ratio increases, and by increasing the storage volume, the ratio decreases.

The heat transfer analysis of boreholes in BTES systems can be analyzed using analytical methods such as the infinite line source (ILS) (Ingersoll & Plass, 1948), infinite cylindrical source (ICS) (Carslaw & Jaeger., 1946), and finite line source (FLS) (Eskilson, 1987; H. Y. Zeng et al., 2002) solutions or numerical methods involving finite difference (FDM) (Lei, 1993; Rottmayer et al., 1997), finite element (FEM) (Kohl et al., 2002; Muraya, 1994), finite volume models (FVM) (Rees, 2000), or a combination of both. However, numerical models are generally not favored due to their computational complexity. Instead, current simulation tools like EED (BLOCON, 2015) and GLHEpro (Spitler, 2000) utilize analytical heat transfer models or pre-calculated numerical solutions known as g-functions. Eskilson (Eskilson, 1987) introduced the g-functions, which are thermal response factors that relate the borehole wall temperature to the ground temperature and heat transfer rate.

Since boreholes in BTES systems are normally connected in series-parallel connections, g-functions cannot be directly applied. Cimmino (2019) used a semi-analytical method to calculate the non-dimensional effective borehole wall temperature, θ_b, or the g-functions of bore fields with mixed parallel and series arrangements. In his method, the borehole wall temperature variations are obtained using the temporal and spatial superposition of the FLS solution combined with a quasi-steady-state solution of the fluid temperature variations inside the boreholes. The resulting g-functions are evaluated using the dimensionless average fluid temperature, $\theta_{f,ave}$, the normalized average heat extraction rate per unit length of borehole, ϕ', and the dimensionless effective bore field thermal resistance, Ω_{field}, which was first introduced by Hellström (1991), as illustrated by Equation 2.

$$\theta_{f,ave}(\tau) = \frac{1}{2}\left(\theta_{f,in}(\tau) + \theta_{f,out}(\tau)\right) = \theta_b(\tau) - \Omega_{field}\phi'(\tau) \qquad (2)$$

In this equation, $\theta_{f,in}$ and $\theta_{f,out}$ are the dimensionless inlet and outlet fluid temperatures of the bore field, Ω_{field} is equal to $2\pi k_g R_{field}$, where R_{field} is the effective bore field thermal resistance, $\tau = 9\alpha_g t/H^2$ is the non-dimensional time, H is the average borehole length, k_g and α_g are the ground thermal conductivity and thermal diffusivity, respectively, and t is the time. Comparisons of the g-functions, θ_b, evaluated by the proposed model and the non-dimensional average storage temperature, θ_s, obtained by the DST model revealed some differences for short time periods. In cases where groundwater flow exists, it may also be necessary to consider the heat transfer between the fluid and the borehole wall using a delta-circuit of thermal resistances (Cimmino, 2015, 2019).

Marcotte and Pasquier (2014) presented a model to determine the thermal response function of boreholes connected in series, parallel, or mixed arrangements. The thermal response function provides the non-dimensional inlet fluid temperature to the bore field instead of the average borehole wall temperature. They evaluated the borehole wall temperatures using the Finite Line Source (FLS) analytical solution and used a linear fluid temperature variation along the pipes. The resulting linear equations are solved to obtain the inlet fluid temperature and the corresponding borehole heat transfer rate at each time step. From these results, the dimensionless unit response function can be calculated and used to estimate borehole inlet temperatures for any heat load scenario.

Other simulation models used for modeling BTES systems are the duct ground storage model (DST) within TRNSYS (Pahud & Hellström, 1996), the superposition borehole model (SBM) (Eskilson, 1987), the combined use of EnergyPlus and GLHEpro (Hsieh et al., 2015), EPS-r (Sibbitt et al., 2012b), and COMSOL (Baser et al., 2016). Among these methodologies, the DST model proposed by Pahud and Hellström (1996) is the most widely used. This model integrates the finite difference method (FDM), analytical solutions, and the superposition principle, resulting in rapid and highly accurate results. In this model, boreholes are distributed uniformly in a cylindrical volume that maintains a vertical symmetry axis, thereby making it impossible to predefine borehole positions or consider arbitrary piping arrangements. This inherent limitation has prompted other researchers to work on novel models that allow the incorporation of independent circuits within boreholes or grant users the ability to specify borehole positions in the bore field (Chapuis & Bernier, 2009; Corentin Lecomte, 2016).

The present study examines two approaches for simulating the thermal performance of BTES systems. The first approach applies a methodology similar to the one presented by Braun (2007) for ice storage tanks. It uses two curves, generated from numerical experiments, that give the heat exchange and storage efficiencies corresponding to the state-of-charge (or discharge) of the BTES. The second model applies a methodology similar to the one presented by Cimmino (2019). However, instead of using the non-dimensional effective borehole wall temperatures, the model uses the non-dimensional average storage temperature.

The objective of developing the first model is to create a user-friendly diagram, similar to the Moody diagram or psychrometric charts, that helps engineers easily estimate specific parameters at certain times or under a certain state of charge (or discharge) conditions. The second approach involves creating a nondimensional diagram, similar to the g-function curve which predicts variations in the average temperature of the BTES over nondimensional time. By accounting for changes in the resistance of the BTES system, the proposed method simulates the performance of the BTES system over time. This diagram can be generated for different design parameters, stored in a database, and subsequently used to simulate the performance of BTES systems. This is similar to how software tools like GLHEpro or EED, which rely on g-function databases, operate. However, here, unlike the g-functions in EED or GLHEpro, the developed diagrams take into account the series-parallel connection of boreholes in a BTES.

Proposed methods

Method #1: Heat exchange (η_{HE}) and heat storage (ξ_{HS}) efficiencies of BTES systems

The heat exchange efficiency of a BTES at time t, $\eta_{HE,t}$, is defined here as a non-dimensional parameter representing the fraction of the heat exchange rate between the fluid and the ground, $\dot{Q}_{exch,t}$, over the total maximum heat that could be exchanged at time t, $\dot{Q}_{max,t}$. This concept follows the standard definition of heat exchanger efficiency for vertical boreholes (H. Zeng et al., 2003).

$$\eta_{HE,t} = \frac{\dot{Q}_{exch,t}}{\dot{Q}_{max,t}} = \frac{\dot{m}\, C_p\left(T_{in,t} - T_{out,t}\right)}{\dot{m}\, C_p\left(T_{in,t} - T_g\right)} = \frac{\left(T_{in,t} - T_{out,t}\right)}{\left(T_{in,t} - T_g\right)} \qquad (3)$$

where $T_{in,t}$ and $T_{out,t}$ are the BTES inlet and outlet temperatures, C_p is the fluid specific heat, $\dot{m}$ is the fluid flow rate, and T_g is the undisturbed ground temperature, which is assumed to be constant.

Equation 3 applies to both charging and discharging modes. A large value of η_{HE} implies that the BTES collects (or discharges) heat at a high rate. Conversely, declining values of η_{HE} imply that the BTES is losing its effectiveness in collecting or releasing heat. The heat exchange efficiency concept used for ice storage tanks is sufficient as these tanks are typically assumed to be adiabatic. In BTES systems, however, heat losses to the surroundings are significant. Therefore, another non-dimensional parameter is required to account for these losses. This parameter, called here the heat storage efficiency, $\xi_{HS,t}$, is defined at time t as the ratio of the heat storage rate, $\dot{Q}_{st,t}$, over the total maximum heat that could be exchanged, $\dot{Q}_{max,t}$:

$$\xi_{HS,t} = \frac{\dot{Q}_{st,t}}{\dot{Q}_{max,t}} = \frac{\dot{Q}_{exch,t} - \dot{Q}_{l,t}}{\dot{Q}_{max,t}} = \frac{Cp_{st} V_{st} \left(T_{s,t} - T_{s,t-1}\right)}{\dot{m}\, C_p \left(T_{in,t} - T_g\right)} \tag{4}$$

where $\dot{Q}_{l,t}$ are the total heat losses from the BTES, $T_{s,t}$ and $T_{s,t-1}$ are the average storage temperatures in the BTES at time t and $t-1$, respectively, $T_{in,t}$ is the inlet temperature at time t, Cp_{st} is the specific heat capacity per unit storage volume, and V_{st} is the storage volume. Note that for the first time step, $T_{s,t} - T_{s,t-1}$ is equal to $T_{s,t} - T_g$.

To define the state-of-charge (or discharge), the storage capacity at time t, denoted as Cap_t, is required. This parameter is evaluated using the inlet fluid temperature prevailing at t, as presented in Equation 5.

$$Cap_t = Cp_{st} V_{st} \left(T_{in,t} - T_g\right) \tag{5}$$

Using this definition, the state-of-charge and discharge are defined by Equations 6 and 7. In Equation 6, the state-of-charge at time t, $x_{c,t}$, is evaluated as the ratio of the stored energy, $E_{st,t}$, over the thermal storage capacity, Cap_t. Alternately, it can also be evaluated by adding the stored energy at the previous time step, $E_{st,t-1}$ to the heat storage rate, $\dot{Q}_{st,t}$, multiplied by the time step Δt, over the thermal storage capacity at time t.

$$\begin{aligned} x_{c,t} &= \frac{E_{st,t}}{Cap_t} = \frac{E_{st,t-1} + \Delta E_{st}}{Cap_t} = \frac{E_{st,t-1} + \dot{Q}_{st,t}\,\Delta t}{Cap_t} = \frac{E_{st,t-1} + \left(\dot{Q}_{exch,t} - \dot{Q}_{l,t}\right)\Delta t}{Cap_t} \\ &= \frac{Cp_{st} V_{st}\left(T_{s,t} - T_g\right)}{Cp_{st} V_{st}\left(T_{in,t} - T_g\right)} = \frac{\left(T_{s,t} - T_g\right)}{\left(T_{in,t} - T_g\right)} \end{aligned} \tag{6}$$

For adiabatic ice storage tanks, x_c reaches a value of 1 at the end of the charging cycle. However, heat losses occur continuously in a BTES. Therefore, the total heat exchanged between the fluid and the ground over a certain period can be greater than the storage capacity. This leads to values of x_c greater than one. To avoid this situation, the heat losses are considered in the evaluation of the state-of-charge and discharge. Equation 7 shows the state-of-discharge definition for BTES systems:

$$x_{d,t} = 1 - \frac{E_{st,t}}{Cap_t} = 1 - \frac{\left(T_{s,t} - T_g\right)}{\left(T_{in,t} - T_g\right)} \tag{7}$$

If the inlet temperature is constant over time, Equation 6 indicates that the storage is fully charged when the average storage temperature reaches the fluid inlet temperature. For cases where the inlet temperature varies, the storage capacity at time t is the amount of heat required to increase (or decrease) the average storage temperature from the ground temperature to the inlet temperature prevailing at time t. This definition of Cap_t helps to develop a strategy that does not depend on the inlet temperature changes but on the state-of-charge of the BTES, x_c, and its complement, the state-of-discharge, x_d. In charging mode, when the BTES is empty, the average storage temperature is equal to the ground temperature with x_c=0 and x_d=1. When charging the storage with a fluid at an inlet temperature higher than the ground temperature, the state-of-charge increases and the state-of-discharge decreases by the same amount. Eventually, when the storage is fully charged, $x_c = 1$ and $x_d = 0$.

In Equations 3 and 4, $\dot{Q}_{max,t}$ can easily be calculated as $\dot{m}$, C_p, T_g, and $T_{in,t}$ are known. It is thus possible to determine $\dot{Q}_{exch,t}$, $\dot{Q}_{st,t}$, $T_{s,t}$, and $T_{out,t}$ if $\eta_{HE,t}$ and $\xi_{HS,t}$ are available. These last two values could be obtained experimentally, but it is more convenient to run numerical experiments on a complete BTES model. The numerical experiments are performed here using the DST model in the TRNSYS environment. However, any complete BTES model could be used. The technique of determining $\eta_{HE,t}$ and $\xi_{HS,t}$ is illustrated using the DLSC project, which was described earlier and whose characteristics are presented in Table 1.

Table 1: Parameters used for the BTES simulation of the DLSC project

Parameter	Symbol	Value	Unit
Borehole depth	H	35	m
Borehole spacing	B	2.71	m
Header depth	D	1	m
Borehole radius	r_b	0.054	m
Outer radius of u-tube pipe	$r_{p,out}$	0.016	m
Inner radius of u-tube pipe	$r_{p,in}$	0.013	m
Center-to-center half distance	S	0.0375	m
Number of boreholes	n_b	144 (24 branches of 6 series boreholes)	-
Ground storage thermal conductivity	k_g	6.048 (1.68)	kJ/hr-m-K (W/m-K)
Fill thermal conductivity	k_{gr}	6.048	kJ/hr-m-K

		(1.68)	(W/m-K)
Pipe thermal conductivity	k_p	1.44 (0.4)	kJ/hr-m-K (W/m-K)
Storage volume	V_{st}	32050	m^3
Storage heat capacity per volume	Cp_{st}	3040	kJ/m^3-K
Borehole resistance	R_b	0.0864	m-K/W
Fluid density	ρ	1000	kg/m^3
Fluid specific heat capacity	C_p	4	kJ/kg-K
Fluid flow rate	$\dot{m}$	28800	kg/hr
Ground and ambient temperature	T_g, T_{amb}	15	℃
Charging/discharging	-	From the center to the periphery/ from the periphery to the center	-

Figure 2 shows the variation of the outlet temperature T_{out}, the heat exchange rate $\dot{Q}_{exch}$, the heat storage rate $\dot{Q}_{st}$, and the total heat losses $\dot{Q}_l$ over time for an inlet temperature of 80 °C. Note that a logarithmic scale is used in Figure 2 so that changes in the first few days could be clearly seen. As can be observed in Figure 2.a, the outlet temperature starts at ~35 ℃ and reaches a *plateau* at ~78 ℃ after ~ 1000 days. In Figure 2.b, $\dot{Q}_{exch}$ and $\dot{Q}_{st}$ are decreasing over time as the average BTES temperature increases and the BTES charges at a lower rate. On the other hand, the total heat losses, $\dot{Q}_l$, increase over time, and when the storage is fully charged, $\dot{Q}_l$ is equal to $\dot{Q}_{exch}$. Figure 2.b shows that the DST model doescalculate heat losses for the first few days of operation (11 days in this example). It assumes that the internally stored heat rate is equivalent to the exchanged heat rate during this time period. Heat losses are accounted for after this initial period and are calculated only at specific time intervals (29 hours in this example). This causes some inaccuracies in the initial days of operation, which can also be observed in in Figure 4.a for η_{HE} and ξ_{HS}, and in Figures A-1b to A-3b.

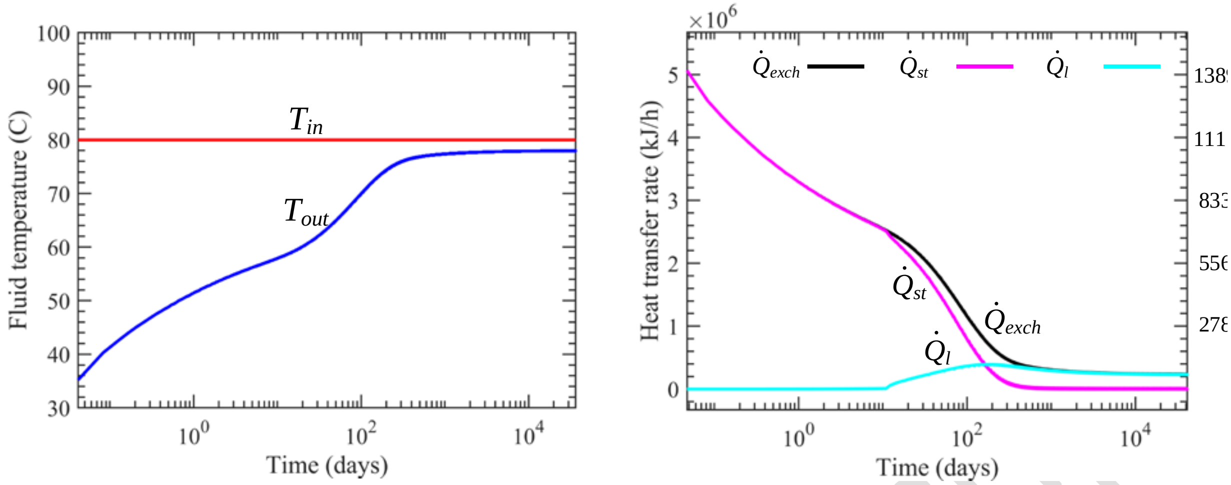

a. b.

Figure 2: a. Variation of the outlet temperature when T_{in} is 80 ℃; b. Variation of the heat transfer rates

Figure 3.a shows the time variation of η_{HE}, ξ_{HS}, and x_c. To obtain these parameters, it is necessary to solve Equations 3 to 6 on an hourly basis. . This assessment can rely on either a constant inlet temperature, as demonstrated here, or a constant heat exchange rate. Figure 3.a demonstrates that the curves for x_c and η_{HE} reach steady-state values after a few years of operation, while ξ_{HS} goes to zero and the storage is almost fully charged with $\dot{Q}_{st}$ ≅0. However, since the BTES is losing heat to the surroundings, the heat exchange rate does not go down to zero and becomes equal to the heat loss rate $\dot{Q}_{exch,t}$= $\dot{Q}_{l,t}$, and so η_{HE} reaches a *plateau* at ~ 0.03 instead of reaching zero. Note that for this condition, $T_s < T_{in}$, which explains why x_c does not reach one.

The time variations of η_{HE} and ξ_{HS} reported in Figure 3.a. can also be represented as functions of x_c, as shown in Figure 3.b by a solid line. The $\eta_{HE} - x_c$ and $\xi_{HS} - x_c$ curves are independent of inlet fluid temperature, ground temperature, and heat exchange rates and identical curves ccan be obained by using different parameters. Using another numerical experiment, the variations of η_{HE} and ξ_{HS} as functions of x_c are evaluated for the same BTES but in discharge mode from the periphery to the center. The result of this experiment is illustrated by a dashed line in Figure 3.b. It can be seen that both η_{HE} and ξ_{HS} are slightly lower than the ones in charging mode. It seems that in discharging mode, where the BTES fluid is injected from the periphery to the center, the BTES loses a little more heat to the surroundings, which is why the values of η_{HE} and ξ_{HS} are lower than those obtained in charging mode.

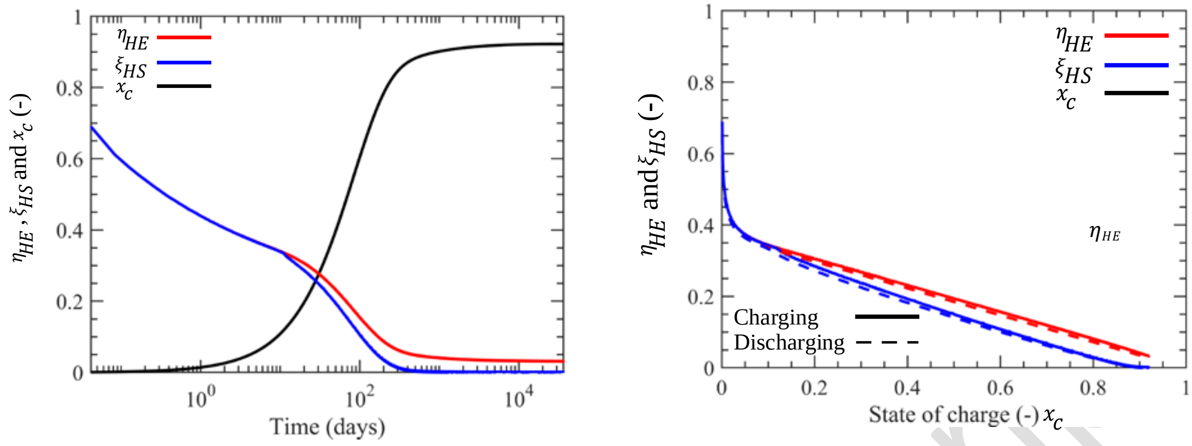

a. b.

Figure 3: a. Variation of η_{HE}, ξ_{HS}, and x_c as a function of time and b. $\eta_{HE} - x_c$ and $\xi_{HS} - x_c$ curves

In this paper, it is assumed that BTES charging is from the center to the periphery and that discharging is from the periphery to the center. Figure 3.b shows that for each BTES, two sets of η_{HE}-x_c and ξ_{HS}-x_c curves related to charging and discharging modes may exist. However, as will be shown with the second method, this difference has an insignificant impact. Thus, when the first method is used, the average of charging and discharging curves is used in calculations.

To summarize, the first proposed method uses numerical experiments on a complete BTES model to generate curves of heat exchange and storage efficiencies as a function of the state-of-charge, η_{HE}-x_c and ξ_{HS}-x_c. Then, these curves can be used to evaluate the outlet temperature from a BTES using simple calculations such as the ones shown in the pseudo-code presented in Figure 4.a for a time-dependent problem and illusttared in Cases 1 to 4. These calculations can be performed with either $T_{in,t}$ or $\dot{Q}_{exch_t}$ as known values. Note that it is assumed that the initial amount of storage, $E_{st,0}$, is zero. By evaluating $E_{st,t}$ and the exchanged heat rate accumulated in the BTES, it is possible to determine the BTES efficiency using Equation 1.

It is also possible to calculate the outlet temperature from a BTES for a given state-of-charge and a known value of either T_{in} or $\dot{Q}_{exch}$. The pseudo-code for these calculations is shown in Figure 4.b. By using the definition of $Cap = Cp_{st}V_{st}(T_{in} - T_g)$, it is also possible to determine how much energy is stored in the BTES at a specific time ($E_{st} =$

$x_c Cap$). The pseudo-codes presented in Figures 4.a and 4.b can also be used for calculations related to the discharging of a BTES using Equation 7.

Known values: f_1, f_2, $\dot{m}$, C_p, T_g, V_{st}, Cp_{st}, T_{in} (or $\dot{Q}_{exch}$)	
10 $t = (t-1) + \Delta T$	
(solve Equations 20 to 80 iteratively until convergence)	(solve Equations 11 to 41 iteratively until convergence)
20 $Cap_t = Cp_{st} V_{st} (T_{in,t} - T_g)$	11 $\eta_{HE} = f_1(x_c)$
30 $\dot{Q}_{max_t} = \dot{m}\, C_p (T_{in,t} - T_g)$	21 $\dot{Q}_{max} = \dot{m}\, C_p (T_{in} - T_g)$
40 $\dot{Q}_{exch_t} = \eta_{HE} \dot{Q}_{max_t}$	31 $\dot{Q}_{exch} = \eta_{HE} \dot{Q}_{max}$
50 $\dot{Q}_{st_t} = \xi_{HT} \dot{Q}_{max_t}$	41 $T_{out} = T_{in} - \dot{Q}_{exch} / \dot{m} C_p$
60 $E_{st,t} = E_{st,t-1} + \dot{Q}_{st_t} \times \Delta T$	51 $Cap = Cp_{st} V_{st} (T_{in} - T_g)$
70 $x_{c,t} = E_{st,t} / Cap_t$	61 $E_{st} = x_c Cap$
80 $\eta_{HE} = f_1(x_{c,t})$, $\xi_{HT} = f_2(x_{c,t})$	
90 $T_{out,t} = T_{in,t} - \dot{Q}_{exch_t} / \dot{m} C_p$	
100 Goto 10 for next time step	
a.	b.

Figure 4: Pseudo-codes used in the first proposed method a. for time-dependent problems; b. for cases where the state-of-charge (or discharge) is known

Application of the first method: Cases 1 and 2

The two cases presented here are based on the DLSC geometry presented earlier (Table 1). In the first case, the fluid inlet temperature is held constant at 50 °C, while in the second case, a constant heat exchange rate of 100 000 kJ/hr (28 kW) is considered. The objective is to compare the outlet temperature obtained with the proposed method and the DST model over a 20-year period. Figure 5 shows the simulation results for these two cases. In this figure, the solid black curves present DST results, while the red dashed lines are results from the proposed method. It can be seen that the inlet and outlet temperatures evaluated with the constant heat exchange rate match perfectly the temperatures determined by the DST model. The outlet temperatures for the constant inlet temperature case have relatively small differences at the beginning and towards the end of the simulation when the storage is fully charged.

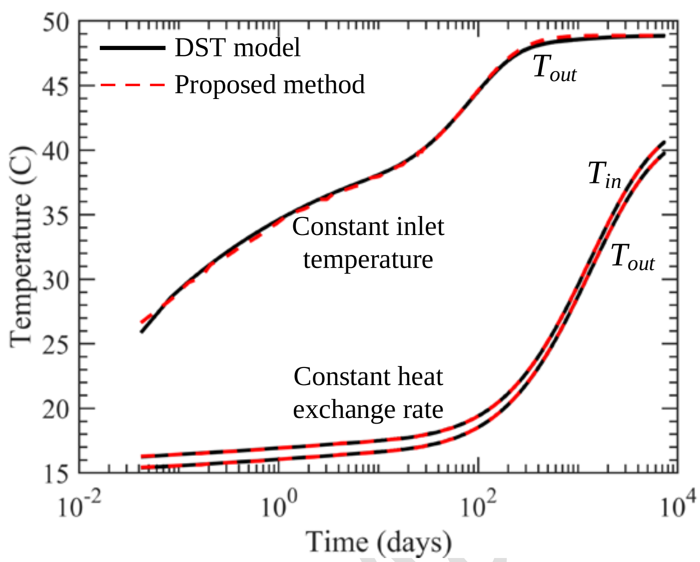

Figure 5: Comparison of the outlet temperature obtained from the first proposed method (dashed line) and the DST model

Application of the first method: Cases 3 and 4

Cases 1 and 2 involved the determination of the outlet temperature based on either a constant inlet temperature or a constant heat exchange rate using the $\eta_{HE} - x_c$ and $\xi_{HS} - x_c$ curves. In Cases 3 and 4, the inlet temperature and the heat exchange rate vary with time, and temporal superposition is thus required. Equations 8 and 9 show how temporal superposition is used when the inlet temperature (Equation 8) or the heat exchange rate (Equation 9) vary.

$$T_{out,t} = T_g + \sum_{j=1}^{t} \left[\left(T_{in,j} - T_{in,j-1}\right) \left(\frac{T_{out,base,t-j+1} - T_g}{T_{in,base} - T_g} \right) \right] \quad (8)$$

where $T_{in,j} - T_{in,j-1}$ in the first-time step is equal to $T_{in,1} - T_g$.

$$T_{out,t} = T_g + \sum_{j=1}^{t} \left[\left(\dot{Q}_{exch,t-j+1}\right) \frac{\left(T_{out,base,j} - T_{out,base,j-1}\right)}{\dot{Q}_{exch,base}} \right] \quad (9.a)$$

$$T_{in,t} = T_{out,t} + \frac{Q_{exch,i}}{\dot{m}C_p} \tag{9.b}$$

where $T_{out,base,j} - T_{out,base,j-1}$ in the first-time step is equal to $T_{out,base,1} - T_g$. In Equations 8 and 9, j is the summation's counter and t is the time step for which the BTES outlet temperature is evaluated. The "base case" is a scenario in which either the BTES inlet temperature or the heat exchange rate is assigned an arbitrary constant value, and its outlet temperature, which varies over time, is solved. Then, the outlet temperature for new scenarios in which either the inlet temperature or the heat exchange rate varies over time are evaluated. This will be further explained in the following sections.

The use of Equations 8 and 9 is illustrated here with Cases 3 and 4, also based on the DLSC geometry. In Case 3, the fluid inlet temperature is assumed to vary from year to year (60 °C, 80 °C, 90 °C, and 50 °C) for four consecutive years. The goal is to evaluate the outlet temperature from the BTES at the end of each year. The solution with a constant inlet temperature of 40 °C is used as a base case. With this constant $T_{in,base} = 40$ °C and applying the $\eta_{HE} - x_c$ and $\xi_{HS} - x_c$ curves, the base outlet temperatures, $T_{out,base}$, can be evaluated for four years of operation and are shown by a blue dashed line in Figure 6.a. Using the base outlet temperatures in Equation 8, the outlet temperatures, T_{out}, can be evaluated. In this problem, there are only four changes over the simulation period. Therefore, only four temporal superpositions are required.

The inlet temperature for the first year is 60 °C. If a time step of one year is considered, then T_{out} at t=1 year is simply given by $15 + (60 - 15)\left(\frac{38.6-15}{40-15}\right) = 57.5$ °C, where 38.6 °C is the outlet temperature determined by considering an inlet temperature of 40°C after one year of operation. This value is indicated by a cross at t=1 year in Figure 6.a. By suddenly raising the inlet temperature to 80°C at the end of the first year, there is a notable increase in the heat exchange rate and rapid rise in the outlet temperature. At t=2 years, the value of the outlet temperature is given by $15 + (60 - 15)\left(\frac{T_{out,base,t}-15}{40-15}\right) + (80 - 60)\left(\frac{T_{out,base,t-8760}-15}{40-15}\right) = 15 + 45\left(\frac{38.9-15}{25}\right) + 20\left(\frac{38.6-15}{25}\right) = 76.9$ °C (second cross in Figure 6.a), where 38.9 °C is the outlet temperature after two years of operation determined by considering the inlet temperature of 40 °C. A similar strategy can be used to obtain T_{out} at the end of the third and fourth years. Hourly calculations were also performed using temporal superposition, as indicated by the green curve in Figure 6.a. It should be noted that these hourly results are identical to the ones obtained with the DST model. The four colored curves (red, yellow, pink, and light blue) represent the temperature evolution obtained after a step change. The green composite curve represents the superposition of the four colored curves.

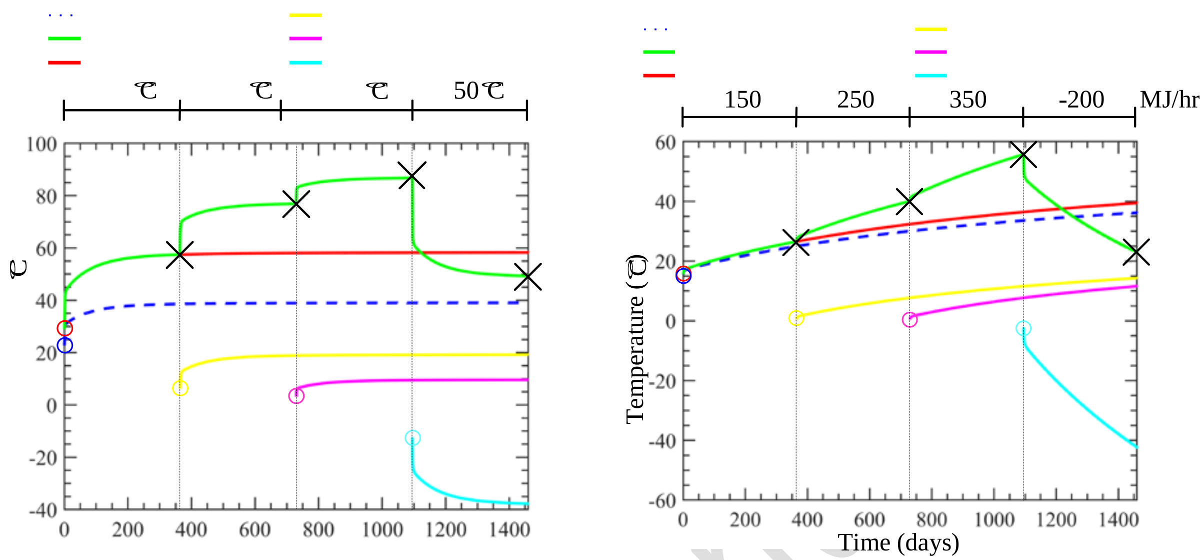

a.   b.

Figure 6: Evaluation of outlet temperatures by the first proposed method for given a. inlet temperature (case 3) and b. heat exchange rate variations (case 4)

In Case 4, the heat exchange rate, Q_{exch}, is assumed to vary from year to year (150000, 250000, 350000, and -200000 kJ/hr) (42, 69, 97, -56 kW) for four consecutive years. Storage from the center to the periphery is assumed for the first three years, while heat is discharged from the periphery to the center in the fourth year. Base calculations are performed with a heat exchange rate of 130000 kJ/hr (36 kW). The resulting inlet and outlet temperatures are evaluated for four successive years by using the $\eta_{HE} - x_c$ and $\xi_{HS} - x_c$ curves. The blue dashed line in Figure 6.b shows the outlet temperature variation evaluated with this base problem.

The outlet temperatures for each time step t corresponding to the four heat exchange rates can be evaluated using the outlet temperatures evaluated for the base load. For the first year, since Q_{exch} is constant, Equation 9.a. simplifies to $15 + \sum_{j=1}^{t}\left[150000\frac{(T_{out,base,j}-T_{out,base,j-1})}{130000}\right]$. In Figure 6.b, this is shown by the green curve for the first year. In the second year, the heat exchange rate is 250000 kJ/hr, and so the outlet temperatures are evaluated using $15 +$

$\sum_{j=1}^{t-8760}\left[250000\frac{(T_{out,base,j}-T_{out,base,j-1})}{130000}\right]+\sum_{j=t-8760}^{t}\left[150000\frac{(T_{out,base,j}-T_{out,base,j-1})}{130000}\right]$. Similar approaches can be used for the third and fourth years. The four colored curves (red, yellow, pink, and light blue) represent the temperature evolution obtained after a step change. The green composite curve represents the superposition of the four colored curves. Here also, the results shown by the green curve are identical to those obtained with the DST model.

As a final note regarding the first method, it should be mentioned that Appendix A examines the influence of the bore field characteristics (borehole height, BTES radius, etc.), geometry, fluid flow rate, and borehole thermal resistance on the $\eta_{HE}-x_c$ and $\xi_{HS}-x_c$ curves.

Method #2: Non-dimensional thermal response factor (θ_s) and thermal resistance (Ω_{field}) of BTES systems

The second method is similar to the ones used for designing regular geothermal bore fields. In these cases, g-functions are used to obtain the borehole wall temperatures for a given heat extraction rate, and the borehole thermal resistances are used to calculate the temperature gradient between the borehole wall temperature and the mean fluid temperature. For BTES systems with boreholes connected with parallel and series circuits, it is possible to relate the mean fluid temperature to the heat extraction rate using a thermal response factor and a bore field thermal resistance. As previously mentioned, Cimmino (2019) and Marcotte and Pasquier (2014) conducted similar studies in this field. However, in contrast to these two studies, the approach proposed here relies on numerical experiments on a BTES model to obtain the non-dimensional thermal response factor (θ_s) and the bore field thermal resistance (Ω_{field}).

As indicated in Equation 10, the non-dimensional average storage temperature, θ_s, is defined using the average storage temperature at a certain time step, $T_{s,t}$, to represent the thermal response of the BTES.

$$\theta_s(t)=\frac{(T_{s,t}-T_g)2\pi k_g L}{\dot{Q}_{exch}}=\frac{(E_{st,t})2\pi k_g L}{(Cp_{st}V_{st})\dot{Q}_{exch}} \tag{10}$$

where $E_{st,t}$ is the accumulated stored energy in the BTES at time t, and L is the overall length of all boreholes (=$n_b H$).

Similar to g-functions, the θ_s-functions depend on non-dimensional time, t/t_s, where $t_s=H^2/9\alpha$, H is the height of each borehole, and α is the ground thermal diffusivity. Figure 7.a shows the θ_s-function for the BTES of the DLSC project as a function of non-dimensional time on a logarithmic scale. This curve is based on numerical results obtained with the DST model. The heat extraction rate and individual borehole thermal resistance were set at 100 000 kJ/hr (28 kW) and 0.1 m-K/W, respectively; the other BTES characteristics are reported in Table 1. The θ_s-function is independent of the heat exchange rates, so the same graph can be obtained with other heat exchange rates as long as it stays constant during the simulation and the BTES geometry is the same. As shown in Figure 7.a, the θ_s-function behavior is similar to the g-functions used in GSHP systems. The value of θ_s is very small for a short non-dimensional time. However, it increases rapidly as borehole-to-borehole interaction increases and tends towards a steady-state value (where the amount of heat exchanged is equal to total heat losses) for large values of the non-dimensional time. As can be seen, the values of θ_s for charging and discharging modes are slightly different, so their average is used in the calculations.

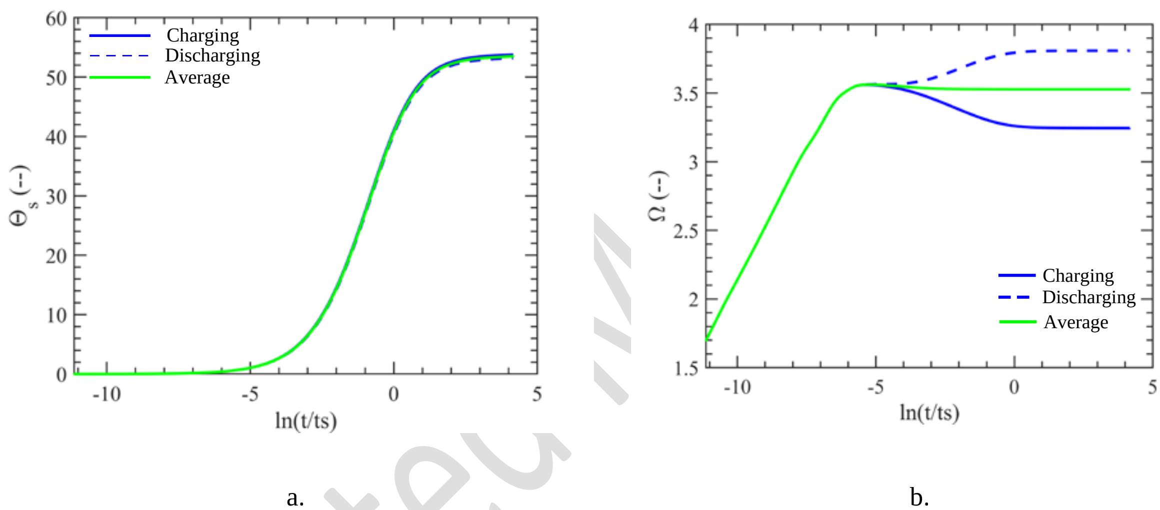

Figure 7: Variation of the a. θ_s and b. Ω_{field} as a function of non-dimensional time obtained for the DLSC geometry

The θ_s-function is not sufficient to fully characterize the BTES. The other required parameter is the bore field thermal resistance, Ω_{field}. This term is similar to the borehole thermal resistance used in the GSHP system, and it relates the average storage temperature to the average fluid temperature in the storage according to the following equation:

$$R_{field}(t) = \frac{(T_{f,t} - T_{s,t})L}{\dot{Q}_{exch}} \tag{11}$$

The bore field thermal resistance is independent of the heat exchange rate, but it varies with time. It can be non-dimensionalized to give $\Omega_{field}(= 2\pi k_g R_{field})$.

Figure 7.b shows the variation of Ω_{field} for the DLSC project when the borehole thermal resistance is 0.1 m-K/W. This figure is evaluated by considering $\dot{Q}_{exch}$=100 000 kJ/hr (28kW) in charging (from the center to the periphery) and discharging (from the periphery to the center) modes. It can be seen that the bore field thermal resistance increases at very early times. This is because the average fluid temperature in the BTES increases, but the average storage temperature has not had time to change significantly ($T_{f,t} - T_{s,t}$, Equation 11). But after a certain period, $T_{s,t}$ starts to increase, and this causes Ω_{field} to decrease slightly and the difference $T_{f,t} - T_{s,t}$ to reach a constant value, leading to a constant value of Ω_{field}. At this stage, Ω_{field} has reached its maximum specific value. In Figure 7.b, this value is about 3.5 and is reached after twenty days (ln(t/ts)≈-5) of operation. After this period, Ω_{field} increases (in discharging mode) or decreases (in charging mode) until it reaches two different constant values. The main reason for this divergence is the small differences between $T_{f,t}$ and $T_{s,t}$ in charging and discharging modes. In Figure 7.b, the temperature difference between charging and discharging modes varies by approximately 0.32°C at the end of operation, resulting in a difference of 0.056 m-K/W in bore field thermal resistance and a difference of 0.6 between the Ω_{field} curves. Preliminary simulation results indicated that the simulated outlet temperature predicted using the charging and discharging curves is almost identical to the result obtained with a simulation performed with an average Ω_{field} curve. This is partly because the second term on the right of Equation 12 is small compared to the first term and has a marginal effect on the prediction of the outlet temperature. Therefore, the average of the charging and discharging curves is used in the results presented later.

In summary, the second proposed method relies on two non-dimensional parameters, θ_s and Ω_{field}, which can be determined using numerical experiments performed on a BTES model. When θ_s and Ω_{field} are known, the average fluid temperature can be determined using the following relationship:

$$T_{f,t} = \frac{T_{in,t} + T_{out,t}}{2} = T_g + \dot{Q}_{exch}\left[\frac{\theta_s(t)}{2\pi k_g L} + \frac{\Omega_{field}(t)}{2\pi k_g L}\right] \tag{12}$$

Appendix A presents variations of θ_s and Ω_{field} with changes in borehole characteristics, geometry, fluid flow rate, and borehole thermal resistance.

The θ_s and Ω_{field} curves presented above are evaluated with constant heat exchange rates. For simulating cases in which the heat transfer rate is variable, temporal superposition is required. Equation 12 can be generalized to account for the effects of load variation with time:

$$T_{f,t} = T_g + \sum_{j=1}^{t} \left(\dot{Q}_{exch,j} - \dot{Q}_{exch,j-1}\right) P_{t-j+1} \quad (13.a)$$

where P_{t-j+1} represents the terms in brackets in Equation 12, $P_{t-j+1} = \frac{\theta_s(t_{t-j+1})}{2\pi k_g L} + \frac{\Omega_{field}(t_{t-j+1})}{2\pi k_g L}$. Finally, the inlet and outlet temperatures can be evaluated using the energy balance in the bore field.

$$T_{in,t} = T_{f,t} + \dot{Q}_{exch}/2\dot{m}C_p \quad (13.b)$$

$$T_{out,t} = T_{f,t} - \dot{Q}_{exch}/2\dot{m}C_p \quad (13.c)$$

Verification of the second method: cases 5 and 6

Two cases are used to verify that the second method can reproduce the DST results and to illustrate the use of the method. In these cases, the DLSC geometry with the design parameters reported in Table 1 is used.

Case 5

Case 5 illustrates how the second method could be used for the preliminary design (i.e. determine the length and number of boreholes) of a BTES with simple calculations. In such preliminary designs, the engineer evaluates the outlet temperature from the BTES for a given set of “worst-conditions” after a certain period. It is suggested that such calculations could be performed using a succession of three load pulses similar to the three pulse technique used to design borehole fields for GSHP systems (Philippe et al., 2010). These conditions could be represented by: i) a consant 10 year pulse with the annual average net load input into the BTES; ii) an average monthly load pulse to the BTES and iii) a six hour peak heat injection (or retrieval) period.

In this example, three successive charging heat load pulses of 100 000, 200 000, and 400 000 kJ/hr (28, 56, 111 kW) with a duration of 10 years, one month, and six hours are used for the DLSC geometry. Equation 14 shows how the resulting average fluid temperatures related to these three heat loads are evaluated.

$$T_{f,1} = T_g + (\dot{Q}_{exch,1} - 0)P_{87600} \tag{14.a}$$

$$T_{f,2} = T_g + (\dot{Q}_{exch,1} - 0)P_{88320} + (\dot{Q}_{exch,2} - \dot{Q}_{exch,1})P_{(88320-87600)} \tag{14.b}$$

$$T_{f,3} = T_g + (\dot{Q}_{exch,1} - 0)P_{88326} + (\dot{Q}_{exch,2} - \dot{Q}_{exch,1})P_{(88326-87600)} + (\dot{Q}_{exch,3} - \dot{Q}_{exch,2})P_{(88326-88320)} \tag{14.c}$$

θ_s and Ω_{field} are evaluated from the average of the curves obtained for charging and discharging modes in Figures A-4.a and A-4.b for B=2.5 m. In equation 14, $\theta_s(t_6)$= 0.01, $\theta_s(t_{720})$= 1.59, $\theta_s(t_{726})$= 1.59, $\theta_s(t_{87600})$= 43.37, $\theta_s(t_{88320})$= 43.49, $\theta_s(t_{88326})$=43.50, and $\Omega_{field}(t_6)$=2.4, $\Omega_{field}(t_{720})$= 3.5, $\Omega_{field}(t_{726})$=3.5, $\Omega_{field}(t_{87600})$=3.5, $\Omega_{field}(t_{88320})$=3.5, $\Omega_{field}(t_{88326})$=3.5 leading to values of the average temperature of 39.5, 42.3, and 44.8℃ after each of the three pulses as shown in Table 2.

Table 2: Considered heat loads, durations, and resulting fluid temperatures for case 5

row	Heat load	Time duration	Time since start of calculation	Outlet temperature
1	100 000 kJ/hr (28 kW)	87600 hr	87600 hr	39.5 ℃
2	200 000 kJ/hr (56 kW)	720 hr	88320 hr	42.3 ℃
3	400 000 kJ/hr (111 kW)	6 hr	88326 hr	44.8 ℃

Case 6

In case #6, a ten-year simulation is performed using the charging/discharging load sequence presented in Figure 8.a. This load is given by $\pm 130000 + \left(sin\left(\frac{2\pi t}{8760}\right) \times \frac{65000}{2}\right)$ in kJ/hr. Here, t represents the time step, " $+$ " corresponds to the first six months of the year indicating the charging mode and "$-$" corresponds to a discharge mode for the second half of the year. Figure 8.b shows the average fluid temperatures determined by the proposed model (shown as the blue solid line curve) and the DST model (represented by the red dashed line curve). The agreement between the results is very good, with a maximum difference between these results of 0.45 °C and a root mean square error (RMSE) of 0.1 °C.

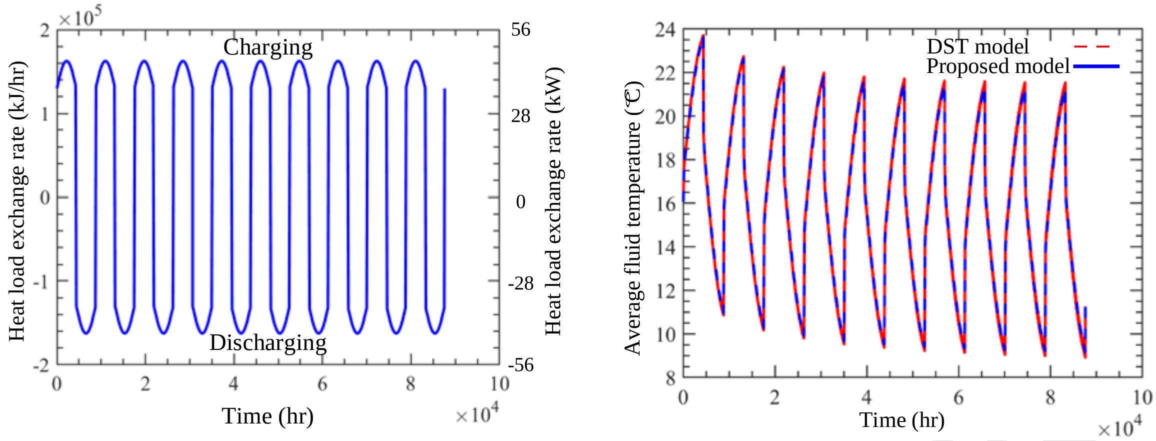

a. b.

Figure 8: Case #6 a. ground loads and b. average fluid temperatures

Relationship between the two methods

This section shows how to calculate the $\eta_{HE} - x_c$ and $\xi_{HS} - x_c$ curves from the θ_s and Ω_{field} curves using an example. From Equation 10, it can be deduced that $T_{s,t} = T_g + \left[\frac{\theta_s(t)}{2\pi k_g L}\right]\dot{Q}_{exch}$, and from Equation 13, it can be concluded that $T_{in,t} = T_g + \sum_{j=1}^{t}(\dot{Q}_{exch,j} - \dot{Q}_{exch,j-1})P_{t-j+1} + \dot{Q}_{exch}/2\dot{m}C_p$, where P_t represents $\left[\frac{\theta_s(t)}{2\pi k_g L} + \frac{\Omega_{field}(t)}{2\pi k_g L}\right]$. Therefore, for the evaluation of $T_{s,t}$ for each time step t, $\left[\frac{\theta_s(t)}{2\pi k_g L}\right]$ should be obtained, and likewise for the determination of $T_{in,t}$ for each time step, $\left[\frac{\theta_s(t)}{2\pi k_g L} + \frac{\Omega_{field}(t)}{2\pi k_g L}\right]$ should be obtained.

As an example, the BTES of the DLSC project with a borehole spacing of 1 m is selected with T_g=15℃ and $\dot{Q}_{exch}$=100 000 kJ/hr (28 kW). The averaged θ_s and Ω_{field} curves are evaluated for a period of 10 years. The θ_s and Ω_{field} curves for $B = 1$ for charging and discharging modes are illustrated in Figure A-4 by blue lines. The θ_s and Ω_{field} curves are used to obtain $\left[\frac{\theta_s(t)}{2\pi k_g L}\right]$ and $\left[\frac{\theta_s(t)}{2\pi k_g L} + \frac{\Omega_{field}(t)}{2\pi k_g L}\right]$ for the 10-year period. This leads to the evaluation of $T_{s,t}$, $T_{in,t}$, and $T_{out,t}$. In return, these three values can be used to obtain the curves of $\eta_{HE,t}$ and $\xi_{HS,t}$ as a function of $x_{c,t}$ (or $x_{d,t}$). Figures 9.a and 9.b. show the curves for $T_{s,t}$, $T_{in,t}$, and $T_{out,t}$, as well as the $\eta_{HE} - x_c$ and $\xi_{HS} - x_c$ curves. By having a specific state-of-charge, x_c (or discharge, x_d), this method can also be used to determine the BTES inlet and outlet temperatures as well as the time required to achieve them without using hourly simulations.

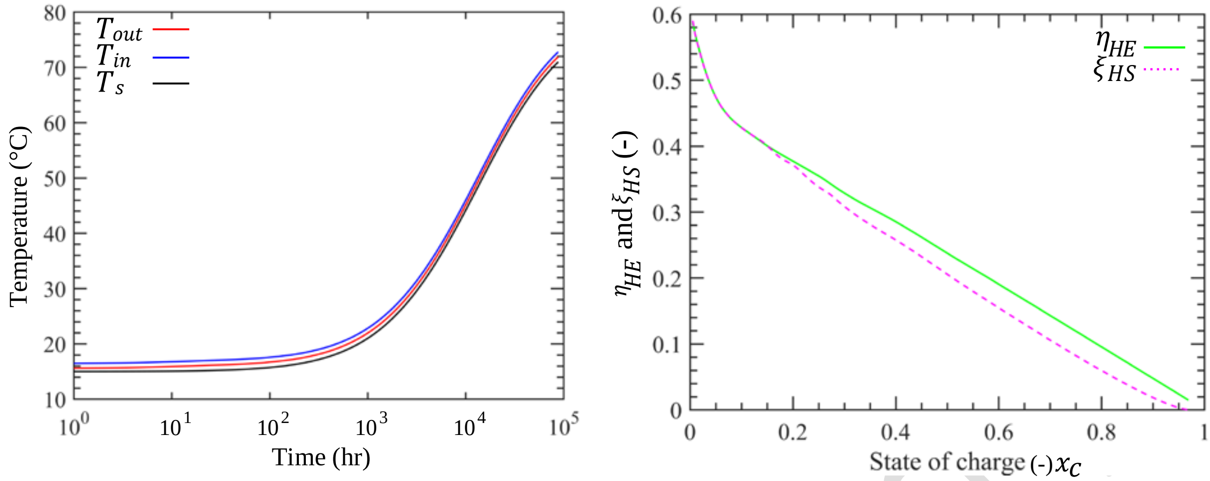

a. b.

Figure 9: Evaluation of $\eta_{HE} - x_c$ and $\xi_{HS} - x_c$ by using the results of the second method

Which of the two methods should be used is problem dependent. If the state-of-charge (or discharge) of the BTES and the inlet temperature or heat exchange rate are known parameters, the first method is preferred. If the goal is to simulate the performance of the BTES on an hourly basis or in response to a few successive pulses of charging (or discharging) heat loads over long time periods, the second method is preferable. This is because evaluations have shown that the first method is sensitive to small variations in η_{HE} and ξ_{HS} parameters over long time periods (or high values of x_c), and η_{HE} and ξ_{HS} vary very little over long time periods, so any inaccuracy in their values may significantly reduce the accuracy of the results.

Once the necessary curves have been calculated, both methods are three to five times faster than running the DST model in the TRNSYS environment. Despite their ease of use and faster calculations, the proposed methods have limitations. First, they require a certain overhead to obtain the necessary curves (Figure 3.b or 7.a and 7.b). Second, even though curves have been developed for several BTES geometries in this paper, a more elaborate database is required so that designers could iterate with various geometries in their designs. Finally, verification of the proposed methods with a tool other than DST would be appropriate.

Conclusion

This paper presents two simplified approaches for simulating the performance of BTES systems. Each method requires two curves that are determined using numerical experiments performed here using the DST model, an established BTES model. Once the curves are determined, it is possible to simulate various scenarios for the considered BTES system. The curves required by the first model show the dependency of heat exchange (η_{HE}) and heat storage (ξ_{HS}) efficiencies as a function of the state-of-charge (x_c), whereas the curves required by the second method show the variations of the non-dimensional average storage temperature (θ_s) and non-dimensional bore field thermal resistance (Ω_{field}) as a function of time.

The proposed methods are not dependent on the use of the DST model to generate the desired curves, and any simulation model capable of simulating the performance of BTES systems can be used to determine the required curves. It is also shown that the two models are inherently linked, and one can obtain curves for one method using the results of the other method. Whenever required, temporal superposition is used to handle situations where the heat supplied to the BTES changes with time. The two models are used in a series of cases. In one of the examples, it is suggested that the design of a BTES could be carried out using three successive thermal pulses, similar to the procedure for determining the ground heat exchanger length in a ground-source heat pump system. This would require very simple calculations and would enable the rapid and accurate design of BTES systems. However, this requires establishing a database of θ_s and Ω_{field} curves (or $\eta_{HE} - x_c$ and $\xi_{HS} - x_c$ curves) evaluated for various BTES systems with different thermal and geometrical characteristics. Using this database and iterating on different lengths or borehole spacings, it would be possible to find a combination of design parameters that meet the minimum and maximum constraints for outlet temperatures from the BTES system.

Credit authorship contribution statement

First author: Conceptualization, Methodology, Software, Validation, Investigation, Writing - Original Draft, Visualization

Second author: Conceptualization, Investigation, Writing - Review & Editing, Supervision, Project administration, Funding acquisition

Declaration of competing interest

There authors declare that they have no known competing financial interests or personal relationships that could have appeared to influence the work reported in this paper.

Acknowledgements

The financial support provided by the Natural Sciences and Engineering Research Council of Canada through a discovery grant awarded to the second author is gratefully acknowledged.

References

Andresen, H. T. (2014). *Study on the performance of central solar heating plants with seasonal storage using underground soil in North China and Norway*. Master's thesis, Norwegian University of Science and Technology (NTNU).

Baser, T., McCartney, J. S., Moradi, A., Smits, K., & Lu, N. (2016). *Impact of a Thermo-Hydraulic Insulation Layer on the Long-Term Response of Soil-Borehole Thermal Energy Storage Systems*. Geo-Chicago.

BlOCON. (2015). *Earth Energy Designer (EED) v3.2*.

Braun, J. E. (2007). A Near-Optimal control strategy for cool storage systems with dynamic electric rates (RP-1252). *HVAC and R Research*, *13*(4), 557–580.

Carslaw, H. S., & Jaeger., J. C. (1946). *Conduction of heat in solids*. Claremore Press.

Chapuis, S., & Bernier, M. (2009). Seasonal storage of solar energy in borehole heat exchangers. *International Building Performance Simulation Association (IBPSA) Conference*, 599–606.

Cho, S., & Mirianhosseinabadi, S. (2013). Simulation modeling of ground source heat pump systems for the performance analysis of residential buildings. *Proceedings of BS 2013: 13th Conference of the International Building Performance Simulation Association*, 1960–1967.

Cimmino, M. (2015). The effects of borehole thermal resistances and fluid flow rate on the g-functions of geothermal bore fields. *International Journal of Heat and Mass Transfer*, *91*, 1119–1127.

Cimmino, M. (2019). Semi-Analytical Method for g-Function Calculation of bore fields with series- and parallel-connected boreholes. *Science and Technology for the Built Environment*, *25*(8), 1007–1022.

Corentin Lecomte. (2016). *Modélisation de champs de puits géothermiques en série pour un stockage thermique saisonnier*.

Eskilson, P. (1987). *Thermal Analysis of Heat Extraction Boreholes*. [Doctoral Thesis, Department of Mathematical Physics], University of Lund, Lund, Sweden.

Gao, L., Zhao, J., & Tang, Z. (2015). A Review on Borehole Seasonal Solar Thermal Energy Storage. *Energy Procedia*, *70*, 209–218.

Gehlin, S. (2016). Borehole thermal energy storage. In *Advances in Ground-Source Heat Pump Systems* (pp. 295–327). Woodhead Publishing.

Hadorn, J.-C. (1988). *Guide du stockage saisonnier de chaleur-Série "Planification, énergie et bâtiments."* Société suisse des ingénieurs et des architectes (SIA).

Hellström, G. (1991). *Ground heat storage: Thermal analyses of duct storage systems I. Theory*. [Doctoral Thesis (monograph), Mathematical Physics], University of Lund, Sweden.

Hsieh, S., Weber, R., Dorer, V., & Orehounig, K. (2015). Integration of thermal energy storage at building and neighbourhood scale. *14th International Conference of IBPSA - Building Simulation 2015, BS 2015, Conference Proceedings*, 2599–2606.

Hughes, P. J. (2008). Geothermal (ground-source) heat pumps: Market status, barriers to adoption, and actions to overcome barriers. *(No. ORNL/TM-2008/232), Oak Ridge National Laboratory (ORNL), Oak Ridge, TN, United States*.

Ingersoll, L. R., & Plass, H. J. (1948). Theory of the ground pipe heat source for the heat pump. *Heating, Piping & Air Conditioning*, *20*, 119–122.

Kohl, T., Brenni, R., & Eugster, W. (2002). System performance of a deep borehole heat exchanger. *Geothermics*, *31*(6), 687–708.

Lanahan, M., & Tabares-Velasco, P. C. (2017). Seasonal thermal-energy storage: A critical review on BTES systems, modeling, and system design for higher system efficiency. *Energies*, *10*(6), 743; 1–24.

Lecomte, C., & Bernier, M. (2016). Modélisation et simulation de puits géothermiques en série pour stockage saisonnier. *Proceedings of the ESim 2016 Conference, May 3-6, McMaster University, Hamilton, Ontario, Canada*, 265–276.

Lei, T. K. (1993). Development of a computational model for a ground-coupled heat exchanger. *ASHRAE Transactions*, *99*(1), 149–159.

Marcotte, D., & Pasquier, P. (2014). Unit-response function for ground heat exchanger with parallel, series or mixed borehole arrangement. *Renewable Energy*, *68*, 14–24.

Mesquita, L., McClenahan, D., Thornton, J., Carriere, J., & Wong, B. (2017). Drake Landing solar community: 10 years of operation. *ISES Solar World Congress 2017 - IEA SHC International Conference on Solar Heating and Cooling for Buildings and Industry 2017, Proceedings*, 333–344.

Muraya, N. K. (1994). *Numerical modeling of the transient thermal interference of vertical U-tube heat exchangers*. Ph.D. Dissertation, Texas A&M University.

Nilsson, E. (2020). *Borehole Thermal Energy Storage Systems for Storage of Industrial Excess Heat: Performance Evaluation and Modelling*. Licentiate degree, Linköping University, Sweden.

Pahud, D. (2002). *Geothermal energy and heat storage*. SUPSI DCT LEEE, Scuola Universitaria Professionale della Svizzera Italiana.

Pahud, D., & Hellström, G. (1996). The New Duct Ground Heat Model for TRNSYS. *Eurotherm - Physical Models For Thermal Energy Stores*, 127–136.

Philippe, M., Bernier, M., & Marchio, D. (2010). izing Calculation Spreadsheet:Vertical Geothermal Borefields. *Ashrae Journal*, *52*(7), 20–28. http://www.freepatentsonline.com/article/ASHRAE-Journal/257352824.html

Rees, S. J. (2000). *An introduction to the finite volume method*.

Rottmayer, S. P., Beckman, W. A., & Mitchell, J. W. (1997). Simulation of a single vertical U-tube ground heat exchanger in an infinite medium. *ASHRAE Transactions*, *103*(2), 651–659.

Schmidt, T., & Hellström, G. (2005). Ground Source Cooling – Working Paper on Usable Tools and Methods. *EU Commission SAVE Program and Nordic Energy Research*, 1–21.

Schulte, D. O., Rühaak, W., Welsch, B., & Sass, I. (2016). BASIMO - Borehole Heat Exchanger Array Simulation and Optimization Tool. *Energy Procedia*, *97*, 210–217.

Sibbitt, B., McClenahan, D., Djebbar, R., Thornton, J., Wong, B., Carriere, J., & Kokko, J. (2012a). The performance of a high solar fraction seasonal storage district heating system - Five years of operation. *Energy Procedia*, *30*, 856–865.

Sibbitt, B., McClenahan, D., Djebbar, R., Thornton, J., Wong, B., Carriere, J., & Kokko, J. (2012b). The performance of a high solar fraction seasonal storage district heating system - Five years of operation. *Energy Procedia*, *30*, 856–865.

Sibbitt, B., McClenahan, D., Onno, T., Thornton, J., Brunger, A., Kokko, J., & Wong, B. (2007). The Drake Landing solar community project: early results. *2nd Canadian Solar Buildings Conference, Calgary (Alberta), Canada*, 1–11.

Spitler, J. D. (2000). GLHEPRO-A Design Tool for Commercial Building Ground Loop Heat Exchangers. *Proceedings of the Fourth International Heat Pumps in Cold Climates Conference, Aylmer, Québec*.

Welsch, B., Rühaak, W., Schulte, D. O., Bär, K., & Sass, I. (2016). Characteristics of medium deep borehole thermal energy storage. *International Journal of Energy Research*, *40*(13), 1855–1868.

Xu, L. (2020). *Design Optimization of Seasonal Thermal Energy Storage Integrated District Heating and Cooling System: A Modeling and Simulation Approach*. [Phd Thesis 1 (Research TU/e / Graduation TU/e), Built Environment]. Technische Universiteit Eindhoven.

Zeng, H., Diao, N., & Fang, Z. (2003). Efficiency of vertical geothermal heat exchangers in the ground source heat pump system. *Journal of Thermal Science*, *12*(1), 77–81.

Zeng, H. Y., Diao, N. R., Fang, Z. H., Ground, T., & Heat, S. (2002). *A Finite Line-Source Model for Boreholes in Geothermal Heat*. *31*(7), 558–567.

Appendix A

This appendix examines the influence of some design parameters on both methods.

Supplementary material for the first method

Borefield characteristics

Results revealed that the buried depth (distance from the ground surface to the top of the boreholes) and the borehole radius have a small effect on the $\eta_{HE} - x_c$ and $\xi_{HS} - x_c$ curves. This is because ambient and ground temperatures are considered equal in the tests, so buried depth has no significant influence on the results, but if they were different, a higher buried depth would improve BTES efficiency. In addition, despite the fact that the effect of borehole radius is very small, it is observed that boreholes with a smaller radius provide slightly better heat exchange and storage efficiencies.

The effects of borehole height and spacing are more significant, as illustrated in Figure A-1. In this figure, the base case (shown by a solid black line) is actually the case presented in Figure 3. The other curves show the influence of doubling (2B) or halving (0.5B) borehole spacing and of increasing borehole height by a factor of 2 (2H) or 4 (4H). It can be seen that longer boreholes with dense spacing have higher efficiencies.

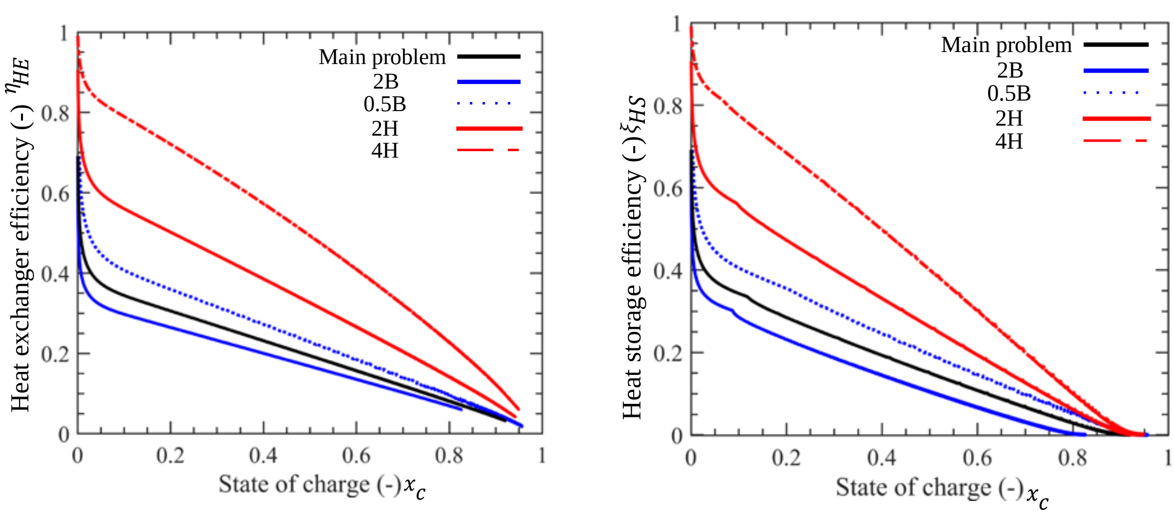

a. b.

Figure A-1: The effects of H and B on the $\eta_{HE} - x_c$ and $\xi_{HS} - x_c$ curves.

Geometry and Fluid flow rate

Figure A-2 shows the effects of geometrical parameters, including the number of boreholes and storage volume, as well as the fluid flow rate, on the $\eta_{HE} - x_c$ and $\xi_{HS} - x_c$ curves. Similarly to Figure A-1, the "main problem" represents the problem solved using the data in Table 1 and illustrated in Figure 3. The other cases are actually handled by utilizing the identical values, with the exception of the parameter whose effects are being investigated, which is multiplied by the values given in Figure A-2. Similar to the relationship between borehole height and spacing shown in Figure A-1, a higher number of boreholes in a smaller storage volume, resulting in smaller spacings, has better efficiency. However, the number of boreholes has a greater impact than storage volume since it influences both storage volume and borehole thermal interactions. Figure A-2 also illustrates that fluid flow rate has a substantial effect on the two curves, with smaller flow rates resulting in higher heat exchange and heat storage efficiencies.

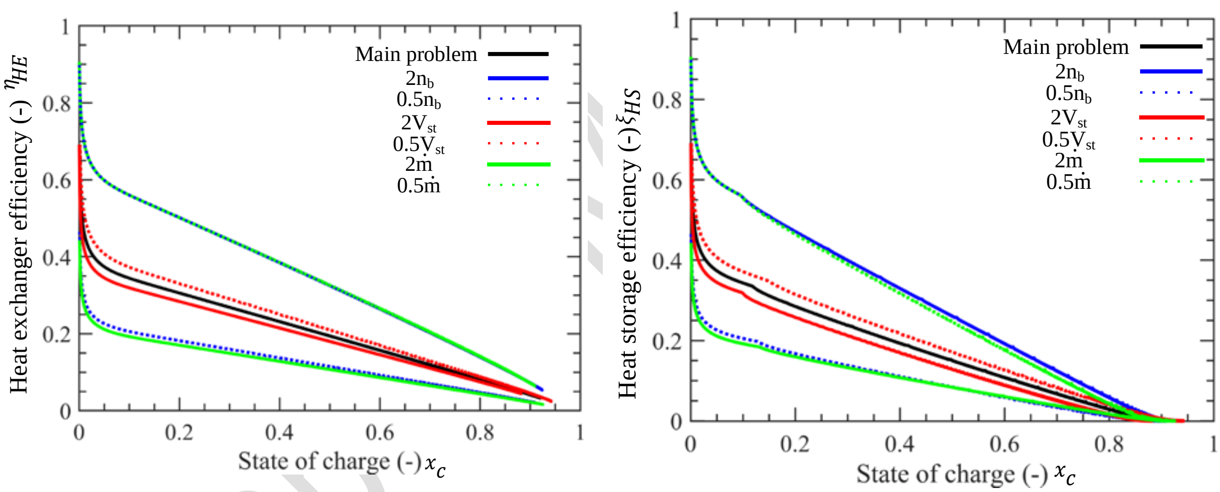

a. b.

Figure A-2: The effects of n_b, V_{st}, and $\dot{m}$ on the $\eta_{HE} - x_c$ and $\xi_{HS} - x_c$ curves.

Borehole thermal resistance

Figure A-3 shows the effects of borehole thermal resistance, fluid specific heat capacity, ground storage, and grout thermal conductivities on the two curves in comparison to the main problem. It can be seen that the ground storage thermal conductivity has the most influence on the two curves, while the grout thermal conductivity has the least. Higher ground or grout thermal conductivities result in higher efficiency. However, larger values of borehole thermal resistance and fluid thermal heat capacity result in lower efficiency. This implies that to obtain highly efficient boreholes, it is necessary to increase the thermal conductivity of the ground or grout while simultaneously decreasing the thermal resistance of the borehole and the thermal heat capacity of the fluid. Finally, the fluid density and the storage heat capacity have negligible influence on the two curves.

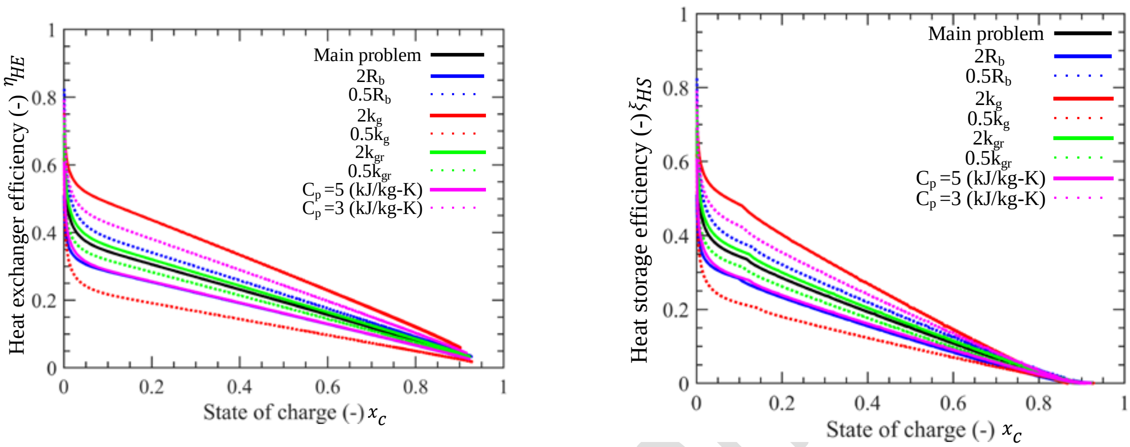

a. b.

Figure A-3: The effects of R_b, C_p, k_g, and k_{gr} on the $\eta_{HE} - x_c$ and $\xi_{HS} - x_c$ curves.

Supplementary material for the second method

Borefield characteristics

In this section, the effects of bore field characteristics, including borehole spacing, borehole buried depth, and borehole length and radius, on θ_s and Ω_{field} are investigated for charging and discharging modes. These comparisons are carried out by considering a constant borehole thermal resistance of 0.1 m.K/W. Figure A-4 shows the effects of borehole spacing. In this figure, the borehole spacing of the DLSC geometry is assumed to vary from 1 to 15 meters, with a corresponding variation of the storage volume set at $\pi n_b H(0.525B)^2$ according to the DST model. In Figure A-4, the results evaluated for the charging mode (from the BTES center to the periphery) are illustrated by solid lines, and the ones evaluated for the discharging mode (from the periphery to the center) are illustrated by dashed lines. As can be seen, the differences in the value of θ_s in charging or discharging mode are not significant. However, the value of θ_s increases significantly when borehole spacing is reduced. For example, for one-meter spacing, after ten years of operation, $ln(t/t_s)$=0.25, the non-dimensional average storage temperature θ_s= 107.6, and by using Equation 10 for a $\dot{Q}_{exch}$=100 000, the corresponding average storage temperature is 71.2°C (= (107.6×100 000/($2\pi k_g$×35×144))+15).

The value of Ω_{field} increases with borehole spacing, as shown in Figure A-4.b. This can be explained by the fact that the difference between the average fluid temperature and the average storage temperature increases with increasing borehole spacing. When the average of both modes is plotted, as was done for $B = 1$ (see dotted line), it can be seen that the average value of Ω_{field} reaches a constant value after its peak.

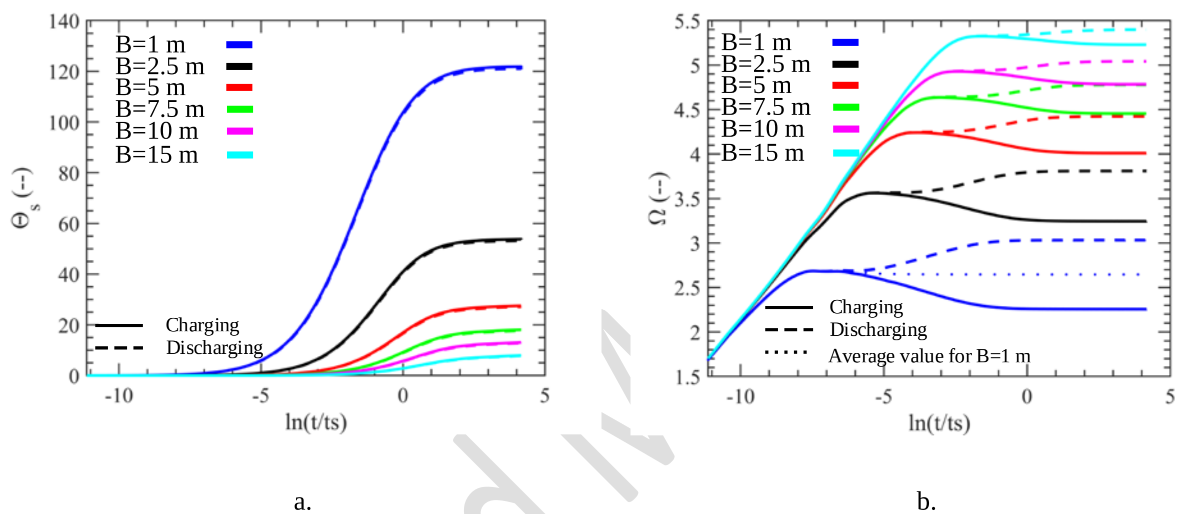

Figure A-4: The effect of borehole spacing on θ_s and Ω_{field}

In Figure A-5, the buried depth (D) is varied from 0.5 to 4.5 m. It can be seen that this affects θ_s and Ω_{field} only for long time periods. Similar to what was explained for the borehole spacing effect, by taking the average of the bore field thermal resistance evaluated for charging (from the center to the periphery) and discharging modes (from the periphery to the center), the "steady-state" bore field thermal resistance can be obtained, which is the one used in calculations.

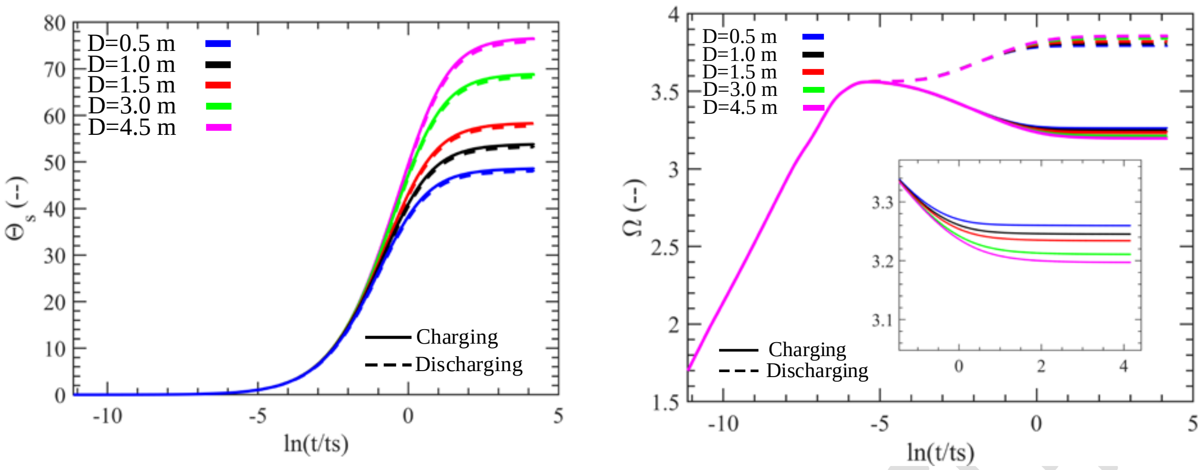

a. b.

Figure A-5: The effect of buried depth on θ_s and Ω_{field}

Figure A-6 indicates the effect of borehole radius on θ_s and Ω_{field} for the DLSC project. It can be seen that θ_s is independent of $ln(t/t_s)$ up to a value of -2. Then, θ_s values are lower for larger borehole radiuses, implying that the average storage temperature is lower for larger boreholes. As for Ω_{field} (Figure A-6.b), an increase in the value of the borehole radius leads to a decrease in the value of Ω_{field}.

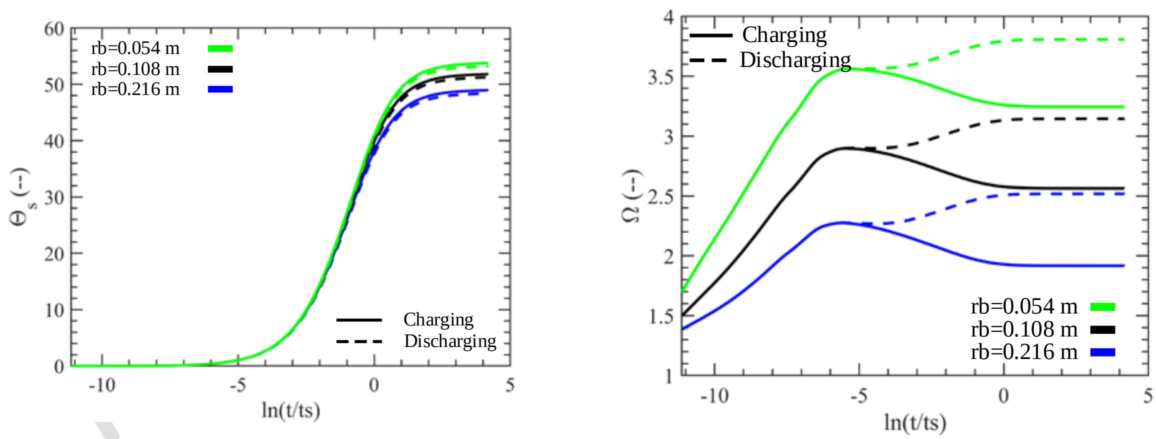

a. b.

Figure A-6: The effect of borehole radius on θ_s and Ω_{field}

Figures A-4 to A-6 are evaluated with 35-meter-long boreholes as installed at the DLSC project. Figure A-7 shows the combined effect of changing borehole height and spacing. In this figure, the storage volume is assumed to change according to $\pi n_b H(0.525B)^2$, as indicated earlier, and the heat extraction rate per unit length of boreholes is considered identical in each case (19.84 kJ/hr per m (5.5 W/m)). The goal is to examine if equal spacing to height ratios, B/H, will result in similar average storage temperatures (θ_s) in the bore field as is the case for g-functions.

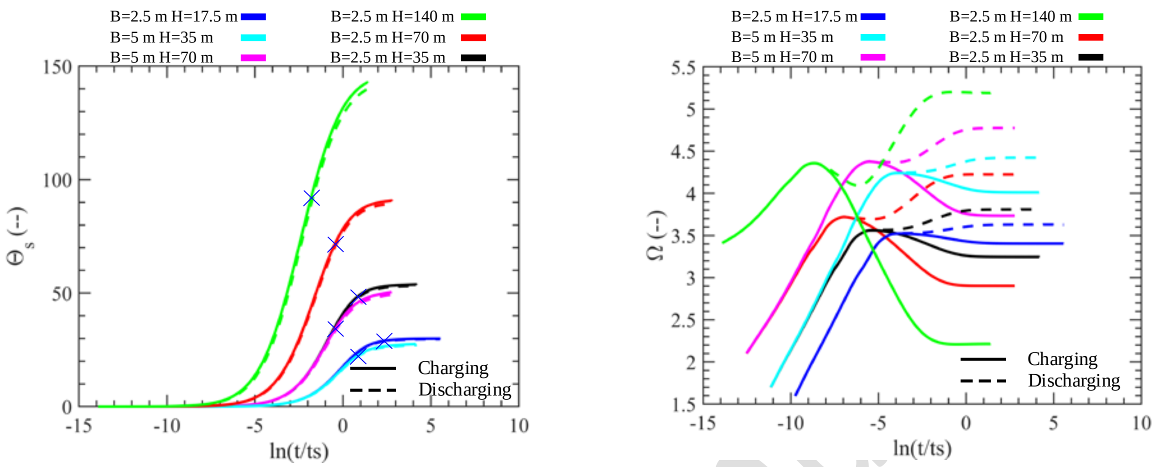

a. b.

Figure A-7 Combined effect of borehole height and spacing on θ_s and Ω_{field}

By analyzing the results, it can be seen that θ_s reaches its steady-state value over a longer period of time when borehole height increases. In addition, cases that have an equal B/H ratio (two bottom curves) have identical θ_s in the beginning, but for long time periods, the average temperature for cases with larger spacing and height is slightly lower. Marks have also been placed on Figure A-7.a to indicate when 20 years of operation have been reached for each configuration. Thus, the difference in the values of θ_s for identical B/H ratios starts to be significant after 20 years. In contrast, in Figure A-7.b, it can be seen that Ω_{field} is significantly different even though the B/H ratio is the same. The thermal resistance of the bore fields that have identical borehole height but different spacing is equal at short time periods, but with increasing time, the bore fields with larger spacing get higher thermal resistance (compare 1- the pink and red curves or 2- the light blue and black curves in Figure A-7.b). For the same borehole spacing, the average of charging and discharging curves remains approximately equal (see 1-dark blue, 2- black, and 3- red curves), but by increasing the borehole height, the average of charging and discharging curves moves in the direction of increasing bore field resistance.

Geometry and fluid flow rate

The effect of the BTES geometry is examined by comparing the results evaluated for three geometries of 6×2, 6×6, and 12×6 (number of parallel branches × number of boreholes in series) with the ones obtained for the 24×6 bore field used in the DLSC project. In this set of results, the heat load, geometry, and mass flow rates are scaled based on the number of boreholes in the bore field so that the boreholes in all scenarios have the same heat load injection per length, borehole height, and spacing.

Figure A-8 shows the θ_s and Ω_{field} evaluated for these four configurations. For evaluation of these results, the θ_s and Ω_{field} of each configuration are evaluated individually for both charging and discharging modes, and then their average is used for illustration. It can be seen that the θ_s depends on the number of boreholes in the bore field, and larger bore fields have higher θ_s due to higher thermal interactions between boreholes. It can also be observed that except for early time periods (<ln(-9)≈8.5 hours), the Ω_{field} of the three bore fields of 6×2, 6×6, and 12×6 is equal to the 24x6 configuration. For the first few hours, the Ω_{field} of the three bore fields is identical, and the source of their difference with the 24×6 configuration in very early time periods is related to the DST model and the fact that it does not report heat loss or heat stored rate variations in the short time periods.

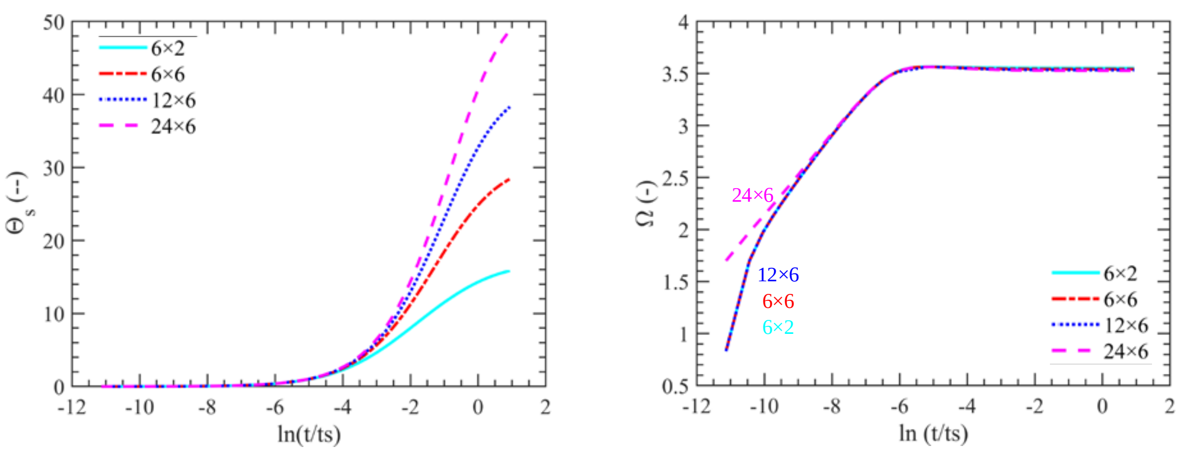

a. b.

Figure A-8: a. θ_s and b. Ω_{field} determined for 6×2, 6×6, 12×6, and 24×6 bore fields

A random charging-discharging ground load (shown in Figure A-9.a) is used to investigate how the average fluid temperature of the 6×2, 6×6, 12×6, and 24×6 bore fields fluctuates over time (shown in Figure A-9.b). This load, which is evaluated randomly by $\left(130000 + \left(sin\left(\frac{2\pi t}{4\times8760}\right) \times \frac{65000}{2}\right)\right) \times \frac{n_b}{144}$ kJ/hr (where t is the time step and n_b is the number of boreholes), is evaluated first for the 6×6 bore field and then scaled based on the number of boreholes in other bore fields and used for ten years of operation. These problems are also solved by the DST model. In Figure A-9.b, the temperatures evaluated by the proposed method are indicated by dashed lines, and the ones determined by the DST model are shown by solid black lines in the background. By looking at Figure A-9.b, it can be seen that the average fluid temperature of larger bore fields is higher since the heat is better trapped in the storage. If these four geometries are considered as four alternative designs, this method can be used to find the optimum design that satisfies the minimum and maximum temperature limits.

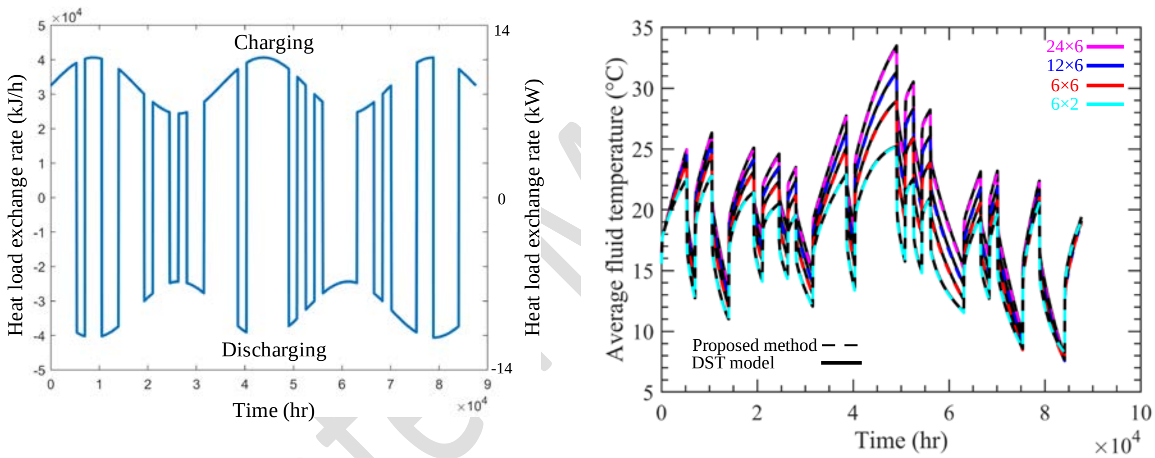

a. b.

Figure A-9: a. Charging-discharging loads used for the 6×6 bore field, and b. the fluid temperature variations determined for the four bore fields

Figure A-10 shows the effect of flow rate on the non-dimensional average temperature and the non-dimensional resistance of the bore field. In this figure, the flow rate reported in Table 1 is multiplied by a constant ranging from 0.1 to 6 while keeping the borehole thermal resistance to 0.1 m-K/W. It can be seen that the change in flow rate has a significant impact on both θ_s and Ω_{field} for both charging and discharging modes. The reason is that the difference between the fluid temperatures and the average storage temperature increases at lower flow rates. However, as the flow rate increases, the difference between the charging and discharging curves becomes insignificant. For example, when the flow rate is increased by a factor of six, the curves for θ_s and Ω_{field} are essentially superimposed over the full range of ln(t/ts) values.

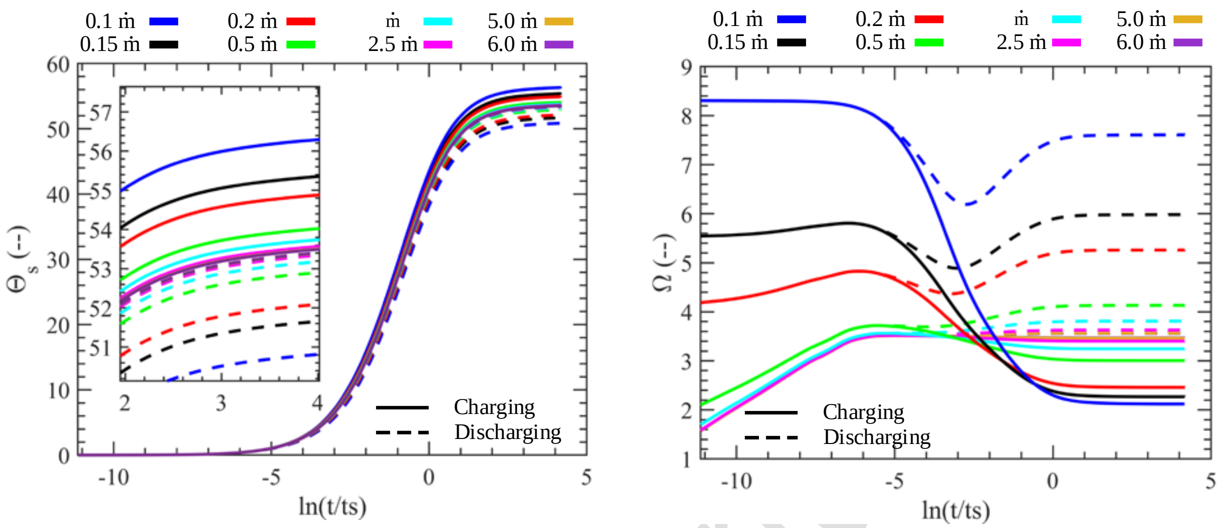

a. b.

Figure A-10: Effect of flow rate on θ_s and Ω_{field}

Borehole thermal resistance

In this section, the effect of the borehole resistance, R_b, on the non-dimensional average storage temperature, θ_s, and the non-dimensional bore field thermal resistance, Ω_{field}, is examined. Five values of borehole thermal resistance are considered: 0.05, 0.075, 0.1, 0.125, and 0.15 m.K/W. The θ_s and Ω_{field} curves, which are illustrated in Figures A-11.a and A-11.b, are obtained by using the DST model for both charging and discharging cycles and by considering a heat extraction rate of 100 000 kJ/hr (28 kW) and a borehole spacing of 2.5 m. The other characteristics of the BTES are reported in Table 1. As explained, both θ_s and Ω_{field} are independent of the heat exchange rates, so identical graphs can be obtained with other heat exchange rates as long as they stay constant during the simulation.

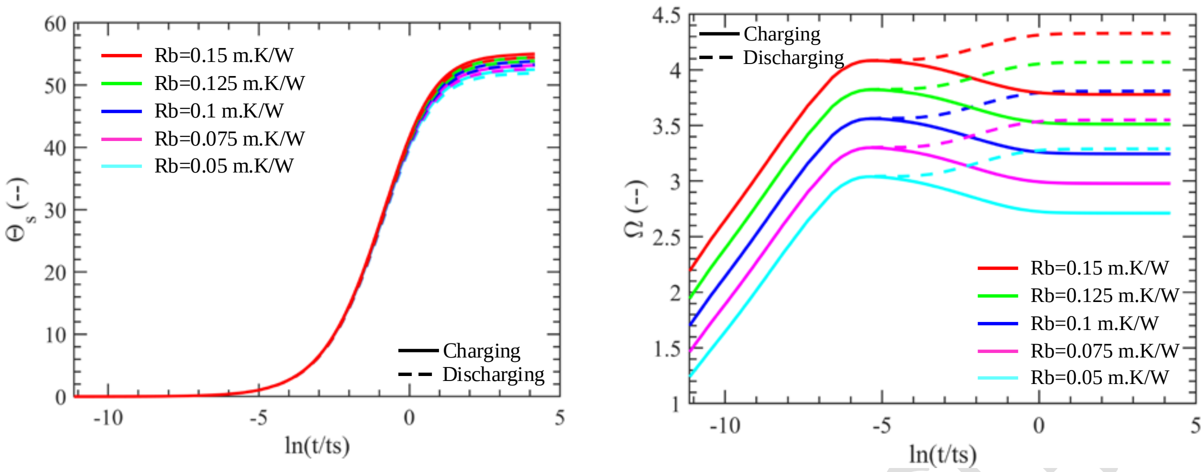

a. b.

Figure A-11: Variation of a. non-dimensional average storage temperature, θ_s, and b. non-dimensional bore field thermal resistance, Ω_{field} curves, due to variation of the borehole resistance, R_b

By looking at Figure A-11.a, it can be seen that the effect of borehole thermal resistance, R_b, on θ_s starts around $1 < \ln(t/t_s)$, which is about four years, and this effect gets bigger with time. The BTES that have a higher R_b have a higher θ_s. The θ_s of the BTES that has R_b=0.15 m.K/W is about 2.5℃ higher than the one with R_b=0.05 m.K/W. This shows that the BTES that have a higher borehole thermal resistance have a higher average temperature and lose less heat. Figure A-11.b shows that the BTES with a higher R_b have a higher Ω_{field}. The average of Ω_{field} for charging and discharging modes of the BTES with R_b=0.15 m.K/W at $\ln(t/t_s) = 4.2$, which is about 96 years, is approximately 4.05 (-), which corresponds to 0.38 m.K/W. The corresponding value for the BTES with R_b=0.05 m.K/W is 0.28 m.K/W.

Nomenclature

A Storage surface area (m^2)

B Borehole spacing (m)

Cap BTES thermal storage heat capacity (kJ)

Cp_{st} Specific heat capacity per volume of the BTES (kJ/m^3-K)

C_p Fluid specific thermal capacity (kJ/kg-K)

D Borehole buried depth (m)

E_{exch} Cumulative exchanged energy with the storage (kJ)

E_{ext} Cumulative extracted energy from the storage (kJ)

E_{inj} Cumulative injected energy in the storage (kJ)

E_l Cumulative energy losses from the BTES (kJ)

$E_{l,b}$ Cumulative energy losses from the bottom of the BTES (kJ)

$E_{l,s}$ Cumulative energy losses from the side of the BTES (kJ)

$E_{l,to}$ Cumulative energy losses from the top of the BTES (kJ)

E_{st} Cumulative energy stored in the storage (kJ)

H Borehole height (m)

k_g Ground thermal conductivity (kJ/hr-m-K)

k_{gap} Gap thermal conductivity (kJ/hr-m-K)

k_{gr} Grout thermal conductivity (kJ/hr-m-K)

k_p Pipe thermal conductivity (kJ/hr-m-K)

L Bore field overall length (m)

$\dot{m}$ Fluid flow rate (kg/hr)

n_b	Number of boreholes (-)
$\dot{Q}_{exch}$	Fluid heat exchange rate (kJ/hr)
$\dot{Q}_l$	Total heat losses from the BTES storage (kJ/hr)
$\dot{Q}_{l,b}$	Heat losses from the bottom of the BTES (kJ/hr)
$\dot{Q}_{l,s}$	Heat losses from the side of the BTES (kJ/hr)
$\dot{Q}_{l,to}$	Heat losses from the top of the BTES (kJ/hr)
$\dot{Q}_{max}$	Maximum heat exchange rate (kJ/hr)
$\dot{Q}_{st}$	Internal heat storage rate of the BTES (kJ/hr)
R_b	Borehole thermal resistance (m-K/W)
R_{field}	Borefield thermal resistance (m-K/W)
r_b	Borehole radius (m)
$r_{p,in}$	Pipe inner radius (m)
$r_{p,out}$	Pipe outer radius (m)
S	Center-to-center shank distance (m)
T_{amb}	Ambient temperature (ºC)
T_{avg}	Annual average temperature of the storage (ºC)
T_b	Borehole wall temperature (ºC)
T_e	Annual average temperature of the environment (ºC)
T_g	Annual average temperature of ground (ºC)
T_{in}	Inlet fluid temperature to the BTES (ºC)
T_{out}	Outlet fluid temperatures from the BTES (ºC)
T_s	Average temperature of the storage (ºC)

t time step, the annual time period (h)

t_{gap} Gap thickness (m)

U Equivalent heat loss factor (kJ/hr-m^2-K)

V_{st} Volume of the BTES (m^3)

x_c State of charge (-)

x_d State of discharge (-)

Greek symbols

α_g Ground thermal diffusivity (m^2/day)

Δ Changes in time step (-)

Δt Time step duration (h)

$\eta_{Borehole}$ Borehole heat transfer efficiency (-)

η_{BTES} BTES overall heat transfer efficiency (-)

η_{HE} Heat exchange efficiency (-)

θ_b Dimensionless effective borehole wall temperature in the bore field, g-function (-)

$\theta_{f,ave}$ Dimensionless average fluid temperature of the bore field (-)

$\theta_{f,in}$ Dimensionless inlet fluid temperature of the bore field (-)

$\theta_{f,out}$ Dimensionless outlet fluid temperature of the bore field (-)

θ_s Dimensionless storage average temperature of the bore field (-)

ξ_{HS} Heat storage efficiency (-)

ρ Fluid density (kg/m^3)

τ Dimensionless time (-)

ϕ' Normalized average heat extraction rate per unit length of borehole (kJ/hr-m)

Ω_{field} Dimensionless thermal resistance of the bore field (-)